repiSalud
Repositorio Institucional en Salud

This is the peer reviewed version of the following article:

Deygas M, Bernard M, Nivoit P, De Belly H, Deslys A, Jakuszeit T, Cuvelier D, Garcia-Gomez M, Barbier L, Wang L, Maurin M, Tejerina E, Baaziz O, Terriac E, Attia R, Kniazeva A, Garbay S, Ortega-Zapero M, Saez A, Gomez-Bris R, Gonzalo P, Gonzalez-Granado JM, Andrés V, Weiner OD, Lennon-Duménil AM, Duménil G, Piel M, Vargas P. Adaptive motility enables neutrophils to rapidly navigate confined capillaries. ***Sci Immunol***. 2026 Sep 4;11(123):eaea1426. doi: 10.1126/sciimmunol.aea1426. Epub 2026 Sep 4. PMID: 42696606.

which has been published in final form at: https://doi.org/10.1126/sciimmunol.aea1426

Title: Adaptive motility enables neutrophils to rapidly navigate confined capillaries

Authors: Mathieu Deygas[1,2]*, Mathilde Bernard[1,2]†, Pierre Nivoit[3]†, Henry De Belly[4,5], Alexandre Deslys[2], Theresa Jakuszeit[1], Damien Cuvelier[1], Moira Garcia-Gomez[2], Lucie Barbier[1,6], Li Wang[1], Mathieu Maurin[7], Emmanuel Tejerina[2], Oumaima Baaziz[2], Emmanuel Terriac[1,8], Rafaele Attia[1,9], Anna Kniazeva[7], Serge Garbay[2], Marina Ortega-Zapero[10,11], Angela Saez[10,12], Raquel Gomez-Bris[10], Pilar Gonzalo[13,14], Jose M. Gonzalez-Granado[10,11,14], Vicente Andrés[13,14], Orion D. Weiner[4,5], Ana-Maria Lennon-Duménil[7], Guillaume Duménil[3], Matthieu Piel[1]*; Pablo Vargas[1,2]*

Affiliations:

[1]Institut Curie and Institut Pierre-Gilles de Gennes, PSL Research University, CNRS, UMR 144; Paris, France.
[2]Leukomotion Lab, Université Paris Cité, INSERM UMR-S1151, CNRS UMR-S8253, Institut Necker Enfants Malades; Paris, France.
[3]Institut Pasteur, Université Paris Cité, INSERM UMR1225, Pathogenesis of vascular infections; Paris, France.
[4]Cardiovascular Research Institute, University of California; San Francisco, CA, USA.
[5]Department of Biochemistry and Biophysics, University of California; San Francisco, CA, USA.
[6]Current address: Center for Interdisciplinary Research in Biology (CIRB), Collège de France, CNRS, INSERM, Université PSL; Paris, France.
[7]Institut Curie, INSERM U932, PSL Research University; Paris, France.
[8]Current address. Cell Polarity, Migration and Cancer Unit, Institut Pasteur, UMR3691 CNRS, Equipe Labellisée Ligue Contre le Cancer; Paris, France.
[9]Current address. Developmental biology laboratory, Sorbonne Université, CNRS UMR7622.
[10]LamImSys Laboratory, Instituto de Investigación Sanitaria Hospital 12 de Octubre (imas12); Madrid, Spain.
[11]Department of Immunology, Ophthalmology and ENT, School of Medicine, Universidad Complutense de Madrid (UCM); Madrid, Spain.
[12]Facultad de Ciencias Experimentales, Universidad Francisco de Vitoria (UFV); Pozuelo de Alarcón, Madrid, Spain.
[13]Centro Nacional de Investigaciones Cardiovasculares (CNIC); Madrid, Spain.
[14]Centro de Investigación Biomédica en Red de Enfermedades Cardiovasculares (CIBERCV); Madrid, Spain.

*Corresponding author. Email: mathieu.deygas@inserm.fr (M.D.)
*Corresponding author. Email: matthieu.piel@curie.fr (M.P.)
*Corresponding author. Email: pablo.vargas@inserm.fr (P.V.)
†These authors contributed equally to this work.

Abstract: To reach inflamed tissues, neutrophils must traverse capillaries as narrow as two micrometers. However, how they do so without compromising blood flow or capillary function has remained unclear. Here, by combining intravital live-cell imaging with biomimetic microdevices, we show that neutrophils maintain migration speed in capillaries across increasing

levels of confinement. This behavior was not shared by other leukocytes and was independent of nuclear properties. Instead, confinement rapidly engaged Rho-dependent actomyosin contractility at the cell rear, thereby offsetting the increased mechanical resistance imposed by confinement. Disrupting this adaptive response caused neutrophil jamming and eventual occlusion of confined capillary-like networks. These findings identify a neutrophil-intrinsic mechanism that couples capillary confinement to rapid migratory adaptation, helping preserve vascular patency and potentially limiting tissue dysfunction during inflammation.

One-Sentence Summary: Neutrophils maintain migration speed in confined capillaries through adaptive actomyosin remodeling.

Main Text:

INTRODUCTION

Neutrophils are the most abundant immune cells in blood circulation, serving as the first line of defense against infections. During inflammation, they act as rapid responders to threats, capable of reaching speeds up to 30 μm/min during inflammation, significantly faster than other cell types (*1*). This remarkable speed reflects their exceptional plasticity, which enables fast displacement in heterogenous tissue microenvironments (*2*). However, excessive recruitment of neutrophils can lead to tissue damage and organ dysfunction (*3*, *4*), thereby making precise control of their recruitment, retention and clearance critical.

Upon tissue injury or infection, circulating neutrophils slow down and crawl on activated endothelium of post-capillary venules, where they eventually stop and extravasate (*5*). Neutrophils also navigate within networks of blood capillaries whose organization and diameters, ranging from 2 to 15 μm, vary between organs (*6*). As a result, neutrophils encounter range of confinement levels and undergo substantial deformation within the narrower capillaries (**Fig. 1A**). In several tissues, including skin and lymph nodes, neutrophils have been shown to migrate independently of blood flow (*7–9*). Within capillaries, neutrophils elongate and must counteract the mechanical resistance imposed by the confinement strength (*10–13*). However, little is known about their capacity to sustain their migration under such microenvironment.

In vivo, impaired neutrophil migration can cause capillary obstruction and tissue damage. In Alzheimer's disease, ischemic stroke, and epilepsy, the arrest of individual neutrophils in brain capillaries contributes to vessel stalling and vascular dysfunction (*14–17*). Similarly, intravascular retention of neutrophils in lung capillaries can generate “trains” of cells, that reduce blood flow and impair tissue oxygenation (*18*). Mechanistic studies of neutrophil migration within narrow vascular spaces have been greatly advanced by microfabricated devices that recapitulate physiological confinement. Using these tools, it was shown that by sensing hydraulic resistance, neutrophils avoid accumulation in dead-ends, thereby facilitate trafficking through complex vessel-like networks (*8*, *19*, *20*). Neutrophils and other leukocytes can also use the nucleus as a sensor to avoid highly confined areas in complex microenvironments (*21*). In neutrophils, their soft nucleus and low level of lamin A/C expression is thought to facilitate their passage through confined spaces (*22*). Nonetheless, the cellular mechanisms that allow neutrophils to migrate through narrow vascular networks without causing obstruction remain largely unexplored.

In this work, we aimed to identify the cellular basis that enables neutrophils to migrate through capillaries. By combining robust single-cell quantification, in vivo live-cell imaging, and in vitro capillary-like microdevices, we identify a cellular mechanism that allows neutrophils to quickly

tune their migration in response to changes in confinement and prevent cell jamming and capillary occlusion in such constrained microenvironments.

RESULTS

Neutrophil migration in skin capillaries is independent of confinement strength

Neutrophils undergo significant deformations when migrating within small blood capillaries. However, the impact of these deformations on their motility remains unknown. To investigate neutrophil migration in confined blood capillaries in vivo, we performed subcutaneous live-cell imaging of endogenous neutrophils in mouse flank skin, where migration within capillaries can occur independently of blood flow during inflammation (*7*). Imaging of the capillary network revealed a parallel array of tubes with diameters ranging from 2.5 to 11.2 µm (median = 3.96 µm) (**Fig. 1, A to C**). In comparison, the median diameter of unconfined neutrophils in the interstitial space was 7.3 µm (**Fig. 1C** and **movie S1**). Local injection of the Gram-negative bacterium *Neisseria meningitidis* (*Nm*) triggered neutrophil accumulation in capillaries, which was evident 1-hour post-treatment (**Fig. 1A** and **fig. S1, A to C** and **movie S2**). In this tissue, no extravasation was detected at the level of capillaries (**movie S3**). These observations indicate prominent neutrophil migration through confining capillaries at early stages of inflammation in skin tissue.

Morphometric analysis of neutrophils within capillaries revealed a broad spectrum of confinement-induced cell deformations, which we quantified using the cell aspect ratio (AR) which was defined as the cell length divided by cell width. (**Fig. 1, D to F**). Whereas some neutrophils appeared nearly round, others were elongated up to tenfold, with an average AR of 6 (**Fig. 1, E and F**). Live-cell imaging of neutrophil migration in capillaries showed that approximately 40% of cells were crawling (speed < 50 µm/min, median speed 22 µm/min) (**Fig. 1G**), 20% were flowing (speed > 50 µm/min), and 40% alternated between flowing and crawling phases (**fig. S1, D to F**). Some neutrophils changed direction within capillaries or migrated against the direction of blood flow, indicating active migration (**movie S4**). In this system, the instantaneous speed of neutrophils was largely independent of the extent of cell elongation (**Fig. 1H** and **movie S3**). Thus, these findings indicate that migration of endogenous neutrophils is not hindered by the confinement imposed by small capillaries in this in vivo system.

Neutrophil migration is independent of confinement strength into in vitro capillaries

Although in vivo results provide valuable insights into neutrophil dynamics in capillaries in a physiological setting, they cannot fully exclude the influence of local inflammatory microenvironmental factors such as adhesion molecules or blood flow. To isolate the effect of physical confinement on neutrophil motility, we used microfabrication to create straight channels with varying cross-sectional areas (ranging from 3 to 8 µm in width and 4 µm in height), mimicking the diameter range of flank skin capillaries observed in vivo (**Fig. 1I** and **fig. S1G**). As a cellular model, we used primary mouse bone-marrow neutrophils matured by treatment with granulocyte-macrophage colony stimulating factor (GM-CSF) (**fig. S1H**) (*23–25*). Mature neutrophils (mNeu) spontaneously entered fibronectin-coated microchannels in the absence of any chemoattractant (**movie S5**). Morphometric analysis showed that the average cell AR ranged from 2.3 in 8 µm-width channels to 9.3 in 3 µm-width microchannels (**Fig. 1J**), values consistent with in vivo measurements (**Fig. 1F**). Nuclear AR also increased with confinement strength, indicating full cellular deformation (**fig. S1I**). Single-cell migration analysis revealed equivalent average speeds across all tested dimensions (approximately 17 µm/min) (**Fig. 1K** and **fig. S1J**). As

observed in vivo, migration speed remained independent of cell AR across channel sizes (**Fig. 1L** and **movie S5**).

We next assessed whether specific adhesion molecules could modulate mNeu migration under different confinement strengths. Channels coated with collagen or Inter Cellular Adhesion Molecule-1 (ICAM-1) supported similar average migration speeds across all geometries (**fig. S1K**). To minimize specific adhesion, we passivated the channels with Pluronic F-127 or Poly-lysin functionalized with poly-ethylene glycol (PLL-PEG). Although these conditions reduced overall migration speed by ~50%, speed remained independent of confinement strength (**fig. S1K**). Thus, mNeu maintain their ability to migrate at different confinement levels regardless of the adhesive substrate, even when basal speed is altered.

Neutrophils maintain migration speed across dynamic changes in confinement

We next examined whether neutrophil migration is affected by dynamic changes in confinement, a scenario that naturally occurs in vivo (**fig. S2A** and **movie S6**). We first analyzed mNeu migration in artificial capillaries featuring an abrupt reduction in width from 6 µm to 3 µm (height of 4 µm) (**Fig. 2A**). As anticipated, entering the narrower section increased cell AR (**Fig. 2, A and B** and **fig. S2B**). Despite this pronounced elongation, mNeu maintained comparable average speeds at the population level in both the wide and narrow regions (**Fig. 2, B and C** and **movie S7**). Only a slight transient decrease in speed occurred during the transition, indicating that cells detect changes in confinement but rapidly recover their migratory pace (**Fig. 2B** and **fig. S2B**). Single-cell analysis revealed heterogeneous responses among individual cells, yet the population-level speed ratio between the two sections remained close to one (**Fig. 2D**). The transition was fast, with 95% of cells crossing in less than 6 min and about 50% in less than 2 min (**fig. S2, C and D**). Primary human blood neutrophils and HL-60-derived neutrophil-like cells (dHL-60) exhibited a slight decrease in cell speed of about 10% in the confined channel section (**Fig. 2E** and **fig. S2, E to G**). When mNeu migrated from narrow (3 µm) to wider (6 µm) channels, speed was also maintained (**fig. S2, H to K**), indicating robustness of migration speed to abrupt changes in confinement.

To further challenge their robustness, we designed channels with alternating 6 µm and 3 µm segments (**Fig. 2F** and **movie S8**). mNeu preserved their average migration speed across all sections, and single-cell analysis revealed consistent crossing times over successive transitions (**Fig. 2, G and H** and **fig. S2L)**. We additionally examined neutrophil motility in funnel-shaped channels whose width gradually decreased from 8 µm to 2 µm over 300 µm or 600 µm (**Fig. 2I**). Morphometric analysis showed a progressive increase in AR as cells migrated toward the narrow end (**Fig. 2J** and **fig. S2M**). In both geometries, mNeu preserved an equivalent migration speed despite the increasing confinement (**Fig. 2J** and **fig. S2M** and **movie S9**), demonstrating sustained migratory performance along smooth confinement gradients. To determine whether this capacity was specific to neutrophils, we analyzed other primary mouse leukocytes in channels featuring an abrupt narrowing from 6 µm to 3 µm. Immature dendritic cells (iDCs), T cells, and natural killer (NK) cells all slowed upon entering the confined section, with single-cell speed ratios of ~0.65, 0.50, and 0.50, respectively (**Fig. 2, K and L**). Thus, these findings demonstrate that primary neutrophils possess a unique, cell-intrinsic ability to maintain migration speed across abrupt, repeated, or gradual increases in confinement strength, a property not shared by other leukocyte populations tested.

Neutrophil migration in confined microchannels is independent of microtubules and nucleus properties

The nucleus is often proposed as a key determinant of cell migration under confinement (*26*). Therefore, we examined neutrophil nuclear shape in capillary-like narrowing. Morphometric analyses of the nuclei of mNeu migrating from 6 µm- into 3 µm- wide channels showed increased elongation and a shift forward relative to the cell body in the confined section (**Fig. 3, A to C** and **fig. S3A**). The microtubule-organizing center (MTOC) was predominantly located within the central opening of the ring-shaped nucleus, slightly posterior to the nuclear centroid, in both wide and narrow channel segments (**Fig. 3, B and C** and **fig. S3A**). In this setting, neither nuclear size nor degree of elongation correlated with the speed ratio (**fig. S3B**). Given the tight association between MTOC and nucleus, we addressed the role of microtubules on cell adaptation to confinement. Microtubule depolymerization with nocodazole increased neutrophil migration speed in both wide and narrow microchannel sections (**Fig. 3D)**. Although a decrease in speed was observed upon transition into the confined region, cells remained faster than control cells within the narrow channels (**Fig. 3D**). However, the speed ratio remained unchanged as compared to control cells (**Fig. 3E**). In addition, microtubule depolymerization resulted in altered nuclear morphology, whose central cavity collapsed upon nocodazole treatment (**Fig. 3F**). These results show that nuclear shape and microtubules are not main determinants of mNeu migration in confined channels, despite nuclear elongation and repositioning under strong confinement.

Nuclear squeezing has been linked to rapid mechano-transduction through a signaling pathway in which Cytosolic Phospholipase A2 (cPLA$_2$) couples nuclear deformation to migratory responses in several cell types, including human neutrophils (*27–29*). Using conditional LysM-Cre; *Pla2g4a*$^{fl/fl}$ (cPLA$_2$-KO), we investigated whether this pathway contributes to maintain mNeu speed under confinement. cPLA$_2$-KO mNeu showed a ~70% reduction in protein expression (**fig. S3C**). Despite this reduction, cPLA$_2$-KO mNeu maintained their speed across confinement transitions to the same extent as control cells, both at the population and single-cell levels (**Fig. 3, G** and **H** and **fig. S3D**). Likewise, pharmacological inhibition using a broad-spectrum PLA$_2$ inhibitor did not impair mNeu speed maintenance (**fig. S3E**). Together, these results indicate that the cPLA$_2$ pathway is not a major determinant of mNeu speed maintenance under varying confinement in microchannels.

Neutrophils have a mechanically soft and deformable nucleus, largely attributed to very low levels of lamin A, which is thought to facilitate passage through confined spaces (*30–32*). To investigate whether nuclear physical properties contribute to confinement adaptation, we assessed migration of mNeu overexpressing lamin A using conditional LysM-Cre; Tg-*Lmna* (Lamin A-OE) (**Fig. 3I** and **fig. S3, F and G**). In LaminA-OE cells, the area of the nuclear central cavity decreased (**Fig. 3J**), showing an impact on nuclear stricture. However, lamin A overexpression did not affect migration speed into 6- or 3-micron-wide channels (**Fig. 3K** and **fig. S3H**). Furthermore, transition-aligned analysis revealed comparable behavior between WT and Lamin A-OE cells (**Fig. 3L**). To further probe lamin A at the single-nucleus level, we used dHL-60 expressing green fluorescent protein (GFP) fused to lamin A (GFP-Lamin A) (**fig. S3I**). These cells also exhibited a comparable migration as compared to control cells in both wide and narrow channel sections (**fig. S3J**). Correlation analysis showed no association between GFP-Lamin A expression and cell speed at the single-cell level (**fig. S3K**). As control, we measured nuclear stiffness upon GFP-Lamin A expression using atomic force microscopy (AFM), which showed a mild increase in nuclear stiffness (**fig. S3, L to N**). Thus, these results show that the ability of neutrophils to sustain high migration speed in confined channels depends neither on passive nuclear properties, such as lamin A expression, nor on active nuclear signaling mediated by cPLA$_2$.

Neutrophils rapidly reorganize their actin cytoskeleton in response to changes in confinement

Previous studies have reported that cells can rapidly reorganize their actin cytoskeleton in response to confinement (*33*–*37*). We therefore investigated whether filamentous actin (F-actin) remodeling accompanies speed maintenance in neutrophils entering narrower channels. Spinning-disk live-cell imaging of mNeu expressing the F-actin binding peptide Lifeact fused to the enhanced GFP (EGFP) protein (Lifeact-EGFP) showed that F-actin was preferentially localized at the cell front in the 6 µm-width section, as previously described for neutrophil-like cells (*38*). In both sections, F-actin was predominantly cortical (**Fig. 4, A and B**). Passage into the narrower section of the channel was accompanied by a fast cortical F-actin shift toward the cell rear (**Fig. 4, A to C** and **fig. S4A** and **movie S10**). This redistribution was confirmed at the population level by averaging Lifeact-EGFP and Phalloidin signals across both channel sections (**Fig. 4C** and **fig. S4, B and C**).

To quantify actin redistribution in individual cells, we calculated the back-to-front actin ratio (BFAR) as a metric (**Fig. 4D**). BFAR values were below 1 in 6-µm section and increased above 1 after cell entry into the narrower section, confirming a front-to-back actin switch (**Fig. 4E**). BFAR elevation coincided with cell elongation (**Fig. 4F**), and we found a positive correlation between the BFAR ratio and the corresponding speed ratio (**fig. S4, D and E**). Consistently, cells unable to concentrate F-actin at the rear failed to maintain migration speed under stronger confinement (**Fig. 4G** and **movie S10**). This F-actin redistribution was reversible: when neutrophils moved from the narrow to the wider section, F-actin rapidly relocalized to the leading edge, mirroring the front-to-back switch observed in the opposite transition (**fig. S4, F to H** and **movie S10**).

To further assess the relationship between actin organization and confinement level, we analyzed cells migrating in straight channels of defined diameters. In channels wider than 5 µm, F-actin remained front-enriched, whereas progressively smaller diameters induced rearward F-actin accumulation (**Fig. 4, H to J** and, **movie S11**). The fraction of cells displaying rear-enriched F-actin increased with confinement (**fig. S4I**). Across all channel widths, migration speed positively correlated with BFAR (**fig. S4J**), indicating that faster cells display more rear F-actin than slower cells at any confinement strength, and that rear F-actin is preferentially used by mNeu in confined channels. Thus, these results show that neutrophils rapidly and reversibly redistribute their actin cytoskeleton in response to confinement changes, with rearward F-actin enrichment occurring specifically when cells enter narrower channels.

Neutrophils dynamically reorganize their actin cytoskeleton in vivo under confinement

To determine whether similar F-actin rearrangements occur in vivo, we transferred Lifeact-EGFP-expressing neutrophils into wild-type recipient mice and induced local flank-skin inflammation. Intravital spinning-disk live-cell imaging revealed mostly elongated neutrophils, consistent with the small diameter of skin capillaries (**Fig. 4, K and L**). In these cells, Lifeact-EGFP was predominantly localized at the cell rear (**Fig. 4, K and L** and **movie S12**), showing backwards F-actin accumulation in neutrophils migrating through confined capillaries in vivo.

We extended these observations to the liver sinusoids during lipopolysaccharide (LPS)-induced endotoxemia (**fig. S4K** and **movie S13**), where capillary diameters were larger and more heterogeneous than in the skin (**fig. S4L**) (*39*). Neutrophils in liver sinusoids displayed lower elongation and an average speed of ~10 µm/min (**fig. S4, M and N**), with F-actin primarily localized at the cell front (**Fig. 4L** and **fig. S4O** and **movie S14**). In rare instances where neutrophils moved from wide to narrow sinusoid segment, we observed a rapid front-to-back redistribution of F-actin, reflecting adaptive remodeling in response to increased confinement (**Fig.**

4M and **movie S15**). Thus, these results demonstrate that neutrophils dynamically reorganize their F-actin cytoskeleton in vivo in response to the confinement strength, mirroring the adaptive rearrangements observed in vitro.

Rho/Myosin II pathway regulates neutrophil migration adaptation to confinement strength

Non-muscle Myosin IIA (MyoII) is a major driver of cell contractility and leukocyte motility (*40*), and contributes to rearward actin localization in fast-migrating leukocytes through increased retrograde actin flows (*41*, *42*). We therefore investigated whether MyoII activation accompanies the F-actin reorganization observed during neutrophil migration under changing confinement.

We first examined subcellular MyoII-GFP localization in primary neutrophils using spinning-disk live-cell imaging (*43*). In these cells, MyoII displayed both diffuse cytoplasmic and cortical punctate localization (**fig. S5A and movie S16**). Cortical MyoII at the cell rear correlated with faster migration speeds (**fig. S5, B to D** and **movie S17**), validating rear MyoII enrichment as a readout of contractile output (*28*, *34*). MyoII-GFP rapidly accumulated at the rear cortex as cells entered the confined section, increasing by ~50% upon full elongation (**Fig. 5, A to D** and **movie S18**). Immunofluorescence of phosphorylated Myosin Light Chain 2 (pMLC2) revealed higher signal in the narrow channel sections **(Fig. 5E** and **fig. S5, E to G**), confirming enhanced MyoII activation. These results demonstrate that neutrophils up-regulate rear MyoII-based contractility in response to confinement strengthening.

Among GTPases, RhoA drives local MyoII activation during cell migration. Therefore, we next monitored RhoA activity using dHL-60 cells expressing the Anillin RhoA-binding domain biosensor fused to GFP (*44*). Cell entry into the narrow channel section triggered a rapid rise in RhoA activity at the extreme cell rear, which was maintained as cells progressed (**Fig. 5, F and G**). By contrast, Rac activity remained front-enriched and unchanged across channel widths (**Fig. 5H**), supporting a selective confinement response through RhoA-MyoII signaling. These results were confirmed through single-cell measurements (**Fig. 5, I and J**).

To test whether RhoA is required for speed maintenance, we performed pharmacological inhibition of the Rho-associated kinase (ROCK), a major downstream effector of RhoA required for MyoII activation. ROCK inhibition reduced neutrophil migration speed in both channel sections but showed a stronger impact in the narrower channels (**Fig. 5, K and L**). ROCK-inhibited neutrophils also required more time to enter the narrow channel segment (**Fig. 5, M and N**). Similar defects were observed upon MyoII ATPase inhibition with blebbistatin (**Fig. 5, K and L**), whereas Myosin light-chain kinase (MLCK) inhibition did not alter neutrophil migration (**Fig. 5L** and **fig. S5H**). We next examined whether ROCK inhibition affects actin remodeling under confinement. Unlike control cells, ROCK-inhibited neutrophils failed to enrich F-actin at their rear when entering the narrow channel (**Fig. 5, N to Q** and **movie S19**). Across straight channels of different widths, ROCK inhibition also prevented the progressive shift of F-actin towards the cell rear (**Fig. 5R** and **fig. S5, I and J**). Together, these data show that the Rho-ROCK pathway mediates confinement-induced MyoII activation and is required for both F-actin redistribution and speed maintenance under strong confinement.

Calcium fluctuations were observed upon cell entering in the narrow channel section (**fig. S5, K and L** and **movie S20**) and were reduced upon extracellular calcium chelation (**fig. S5M**). However, chelation of extracellular or intracellular calcium, the blocking of calcium-activated chloride channels, or the inhibition of stretch-activated calcium channels, did not impair the ability of mNeu to sustain their migration speed under strong confinement (**fig. S3F** and **fig. S5, N to Q**). Similarly, depletion of Rictor or mSin1, two mediators of mTORC2-mediated Rho activation

through membrane tension, did not impair this process (**fig. S5R**) (*44*, *45*). Thus, our findings show that neutrophil migration adaptation to confinement relies on a RhoA-ROCK-MyoII contractility pathway that operates independently of calcium dynamics, probably through a noncanonical signaling pathway.

ROCK is essential for efficient neutrophil trafficking in complex capillary-like networks

During migration into inflamed tissues, neutrophils often encounter highly intricate capillary networks, such as those found in the liver (**fig. S4K**). To assess how physical confinement affects neutrophil migration in these complex microenvironments, we engineered networks of interconnected microtubes with varying diameters (3, 4, 5, and 6 μm) (**Fig. 6, A to D**). In this in vitro system, mNeu entered the tubes spontaneously and maintained similar average migration speeds across all sizes, despite frequent directional changes at network bifurcations (**Fig. 6D** and **movie S21**). In this system, network exploration by neutrophils was consistent across different levels of confinement, as indicated by comparable mean squared displacement (MSD) values (**Fig. 6E**). These findings demonstrate that neutrophils can efficiently navigate complex channel networks composed of segments with diverse diameters.

To further investigate the importance of migration adaptation to confinement, we inhibited ROCK focusing on the most restrictive (3 μm-wide) channels network. As previously observed in straight channels, ROCK inhibition reduced neutrophil migration speed (**Fig. 6F**). This reduction was accompanied by a decrease in the MSD, showing a diminished capacity to explore the confined network (**Fig. 6G**). Kymograph analyses confirmed slower migration and revealed more frequent directional changes following ROCK inhibition (**Fig. 6H**). This was further supported by a reduction in the angular autocorrelation (AAC) function, reflecting decreased directional persistence (**Fig. 6I**). Collectively, these results establish that ROCK activity is critical for optimal navigation and persistent movement within confined capillary-like networks.

All analyses above were performed during the first five hours of imaging, when neutrophils could be tracked as individual cells. At later time points, however, progressive cell accumulation occurred in specific regions of the network, accompanied by an overall increase in neutrophil density (**Fig. 6J** and **movie S21**). While control cells continued to navigate efficiently even at high local densities, ROCK-inhibited neutrophils formed stable, slow-moving multicellular “trains” within confined segments (**Fig. 6, J and K**). To quantify this phenomenon, we calculated the average nearest-neighbor distance between neutrophils for each segment at each time point, as a proxy for local cell density. The analysis showed a marked increase in local cell density upon ROCK inhibition (**Fig. 6L**), resulting in prolonged residence within individual segments. These results are consistent with persistent accumulation and impaired clearance, a behavior reminiscent of cell jamming (**Fig. 6M**). However, this behavior was not observed in networks of 6 μm-wide channels, either in control or in ROCK-inhibited mNeu (**movie S21**).

Thus, these data demonstrate that inhibition of ROCK activity in network of narrow channels leads to neutrophil slowing down, reduced directional persistence, and eventual accumulation and retention. This suggests that the ability of neutrophils to adapt their migration speed to strong confinement is essential for efficient trafficking through capillary networks, thereby helping to prevent cell jamming during episodes of massive neutrophil recruitment, such as during inflammation.

DISCUSSION

To perform their functions, neutrophils must rapidly migrate through diverse microenvironments, including highly confined vascular spaces. Here, we identify a neutrophil-intrinsic mechanism that enables efficient transit through narrow capillaries both in vivo and in vitro. Although neutrophils are often assumed to rely mainly on their exceptional deformability, our data indicate that fast active remodeling of the actomyosin cytoskeleton through the Rho-MyoII axis is a main determinant of their migration under strong confinement. Neutrophils maintained their migration speed across a broad range of capillary dimensions and through abrupt, repeated, or gradual changes in confinement, a behavior not observed in the other leukocyte populations tested. Functionally, disrupting this adaptive response promoted progressive neutrophil accumulation and jamming in confined capillary-like networks, suggesting that rapid motility adaptation may help neutrophils access highly restricted vascular regions while limiting capillary obstruction during inflammation.

The neutrophil nucleus is widely considered a key factor enabling migration through narrow spaces because of its segmented shape, low lamin A levels, and high deformability (*30–32*). Our results confirm that neutrophil nuclei undergo substantial shape remodeling under confinement, yet indicate that nuclear properties are not the primary determinants of speed maintenance within capillaries. Indeed, increasing lamin A expression in primary neutrophils and dHL-60 cells did not impair migratory adaptation, despite measurable effects on nuclear shape and stiffness. This results is consistent with a previous report showing that the contribution of lamin A to cell migration is context dependent (*46*). Moreover, lamin A imaging during AFM measurements indicated that the nuclear envelope remained not fully tensed even under two micrometer confinement, suggesting that neutrophils retain excess nuclear lamina. In line with this observation, a recent study proposed that the nuclear envelope becomes limiting for migration through highly confined spaces only once it is fully stretched (*47*). Thus, incomplete unfolding of the nuclear envelope may explain the absence of a detectable effect of nuclear shape change and lamin A overexpression on neutrophil migration in confined microchannels.

Leukocyte migration is classically understood to depend on front-rear polarity, with F-actin polymerization at the leading edge and actomyosin contractility at the rear driving cell movement in vitro and in vivo (*42*, *44*, *48–50*). In multiple cellular systems, rearward enrichment of F-actin and MyoII is associated with faster migration (*48*, *49*, *51–55*). Our results extend this framework by showing that rapid enhancement of actomyosin contractility can offset the mechanical resistance imposed by capillary confinement during spontaneous migration of mouse and human neutrophils. Although confinement-induced increases in contractility have been described previously (*27*, *28*, *56–58*), our findings reveal in neutrophils an exceptional degree of tuning that approaches a “perfect adaptation” phenotype: despite substantial environmental constraints, these cells maintain near-constant migration speed through rapid, active adjustment of their migratory machinery, indicative of true adaptation rather than passive insensitivity.

Several mechanosensitive pathways have been shown to regulate the leukocyte actomyosin cytoskeleton in response to confinement. For example, $cPLA_2$ has been identified as a sensor of nuclear-envelope tension (*27–29*, *59*, *60*). However, neither $cPLA_2$ depletion in $cPLA_2$-KO cells nor its pharmacological inhibition impaired neutrophil migration in confined capillaries. Membrane tension has also been reported to regulate neutrophil actomyosin through mTORC2-dependent signaling and Rho activation (*44*, *45*, *61*, *62*). Yet, depletion of core mTORC2

components Rictor and mSin1 in dHL-60 cells did not impair migration speed in confined capillaries. In addition, inhibition of calcium dynamics did not affect migratory adaptation to confinement. Together, these observations indicate that the mechanisms enabling neutrophils to adapt to changing confinement differ from those described in other leukocyte populations. In line with these results, a recent study indicates that neutrophils respond to confinement through F-actin remodeling mechanisms distinct from those described in T cells and dendritic cells (*63*, *64*). One possibility is that in neutrophils, adaptation to confinement arises in part from a purely geometric effect: as cells elongate, their surface-to-volume ratio increases, potentially promoting interactions between cytosolic Rho GTPases and membrane-associated GEFs (*65*). Although difficult to test directly, such geometric constraints could contribute to the rapid activation of contractility observed under confinement and may help explain the precise adaptation of migration to both gradual and abrupt changes in confinement. Defining the molecular basis of this rapid, noncanonical Rho-MyoII activation in neutrophils will be an important direction for future research. The lack of a defined upstream mechanism remains a key limitation of the present study.

During inflammation, large numbers of neutrophils accumulate within capillary beds. When these cells become immobilized, either individually or as multicellular clusters, blood flow can be compromised, thereby impairing tissue oxygenation. Neutrophil-mediated vascular obstruction has been documented in inflammatory settings in the lung (*18*, *66*), as well as in the brain in pathologies including Alzheimer's disease, ischemic stroke, and epilepsy (*14–17*). The ability to adapt migration to capillary confinement may therefore represent a physiological requirement during inflammation, enabling large numbers of neutrophils to rapidly infiltrate highly confined capillaries while limiting the formation of plugs and tissue damage. Whether defects in this adaptive program directly contribute to vascular dysfunction in vivo and whether distinct neutrophil subsets differ in their capacity to respond to changes in confinement, as reported for T cell subsets (*67*), remain important questions for future studies.

MATERIALS AND METHODS

Study design

This study was designed to determine how neutrophils migrate through confined blood capillaries. We combined intravital live-cell imaging with custom microfabricated devices to analyze, at single-cell resolution, migratory behavior and cytoskeletal dynamics in neutrophils. Experiments involving mice (both male and female) or isolated neutrophils were randomly assigned to experimental groups, without investigator blinding, and no outliers were excluded from the analyses. For migration assays in microchannels with abrupt size transitions, one transition event was analyzed per cell, and neutrophils that failed to enter the constricted region were excluded. Key findings were validated in neutrophils from human donors and in additional murine immune cell types. Sample sizes, numbers of independent experiments and statistical tests are provided in the figure legends.

Mice

Male and female mice on a C57BL/6J (B6) genetic background were used at age ranging from 6 to 16 weeks, sex-matched where possible. C57BL/6J (WT) mice (obtained from Charles River (jax #00664)), Lifeact-EGFP (enhanced green fluorescent protein) mice (*68*), MyoII-GFP (green fluorescent protein) mice (*43*), were housed under pathogen-free conditions within the animal research facilities of the Institut Curie and SFR Necker, in compliance with the European and French National Regulation for the Protection of Vertebrate Animals used for Experimental and other Scientific Purposes (Directive 2010/63; French Decree 2013-118). cPLA$_2$-KO (LysM-

Cre;*Pla2g4a*$^{fl/fl}$) mice were shared by Ana-Maria Lennon-Duménil (Institut Curie, France) (*60*). Lamin A overexpression (Lmna-OE) mice (LysM-Cre;Tg-*Lmna*) were shared by Jose M. Gonzalez-Granado and Vicente Andrés (CNIC, Spain). Briefly, Tg-*Lmna* mice were generated using CRISPR/Cas9-directed mutagenesis by insertion of two copies of the mouse *Lmna* cDNA into the *Rosa26* locus (*69*). Its expression was regulated by the CAG (CMV early enhancer/chicken β-actin promoter with rabbit β-globin intron) promoter, followed by a stop signal flanked by LoxP sequences, prior to the *Lmna* cDNA. Lamin A overexpression was obtained by crossing with the LysM-Cre mice (*70*), which deleted the LoxP flanked stop codon to trigger the overexpression of the two *Lmna* copies in neutrophils and macrophages. For migration analysis, we compared neutrophils from LysM-Cre^{+};Tg-*Lmna* to LysM-Cre$^{-/-}$;Tg-*Lmna* as control. All mouse strains did not exhibit a harmful phenotype and were euthanized by cervical dislocation by appropriately trained and qualified personnel.

Human samples

Whole venous blood from two distinct healthy donors was obtained from the Établissement Français du Sang (EFS, convention CCPSL 2024-2027-001). Blood was collected in heparin tubes and supplemented with 1 mM Ethylenediaminetetraacetic acid (EDTA) (Gibco, 15575) prior to processing.

Cell isolation and culture

Murine primary cells

A single-cell suspension was prepared from mouse femur and tibia's bone marrow. Mouse neutrophils were isolated using the Mojosort neutrophil isolation kit (BioLegend, 480058) following the manufacturer's instructions. Expression of surface markers of neutrophils were analyzed by flow cytometry to assess the sample purity. Neutrophil enrichment was assessed by flow cytometry analysis of Ly6G and CD11b expression. After isolation, neutrophils were cultured overnight at a concentration of 1×10^6 cells/ml in Roswell Park Memorial Institute (RPMI) 1640 Medium (Thermo Fisher Scientific, 11875093) supplemented with 10 % fetal bovine serum (Biowest, S1810), 100 U/ml penicillin-streptomycin (Thermo Fisher Scientific, 15140122), 20 mM HEPES (Gibco, 15630056), and 50 ng/ml recombinant granulocyte-macrophage colony-stimulating factor (GM-CSF) (Peprotech, 315-03-20UG).

For murine bone marrow derived dendritic cells (BMDCs), murine Natural-killer cells (NK cells), murine T cells, please refer to the Supplementary Materials and Methods for further information.

Human neutrophils

Human neutrophils were isolated by immunomagnetic negative selection using the EasySep Direct Human Neutrophil Isolation Kit (STEMCELL Technologies, 19666) according to the manufacturer's instructions. The purity of the isolated neutrophils was assessed by flow cytometry. Samples were analyzed for the expression of surface markers CD16 and CD66b, with enrichment defined as the percentage of CD16^{+}/CD66b^{+} cells. After isolation, neutrophils were resuspended in RPMI 1640 medium supplemented with fetal bovine serum (10 %), penicillin-streptomycin (100 U/ml) and HEPES buffer.

Intravital experiments

For intravital imaging, experiments were performed at Institut Pasteur in agreement with guidelines established by the French and European regulations for the care and use of laboratory animals and approved by the Institut Pasteur Committee on Animal Welfare (CETEA) under the

protocol code CETEA 230080. C57BL/6 male and female mice were used at age ranging from 6 to 14 weeks and were housed under standard conditions (light 07.00 to 19.00 h; temperature 22 ± 1 °C; humidity 50 ± 10%) within the animal facility of the Institut Pasteur.

At 30 min prior to intravital imaging, mice were injected subcutaneously with buprenorphine (0.05 mg/kg of body weight) and anesthetized by spontaneous inhalation of isoflurane (induction: 4%; maintenance: 1.5%) vaporized in 100 % O_2 (0.3 L/min). Mouse hydration and body temperature were respectively maintained by intraperitoneal injection of 200 µl of 0.9% saline solution every hour and with a 37 °C–heating pad. Labeled antibodies (Table S1) were injected intravenously 15 min prior to imaging, consisting of 5 µg of anti-Ly6G conjugated with Alexa-Fluor 488, 594 or 647 to label circulating neutrophils and 10 µg of anti-CD31 conjugated with Alexa-Fluor 488, 594 or 647 to label the vasculature. Mice were imaged for up to 4 hours.

For infected dorsal back skin observations, mouse preparation was conducted as previously described (*71*). Using Nanofill Syringe (World Precision Instruments), 3 intradermal injections of 1 µl wild-type strain *Neisseria meningitidis* bacterial suspension (1×10^8 Colony Forming Unit/ml) were made (*7*). For liver observations, organ preparation was conducted as previously described (*72*). Mice were treated with an intraperitoneal injection of purified LPS from *E. coli* (1 mg/kg of body weight) 2 hours prior to intravital microscopy. For F-actin imaging in dorsal back skin and liver, purified bone-marrow Lifeact-EGFP expressing neutrophils (100 µl, 7.5×10^6 cells) were injected intravenously 3 hours prior to imaging.

Microfabricated devices

All microdevices used for this work were designed and prepared by photolithography. Please refer to the Supplementary Materials for further information about device preparation, coating and loading**.**

Microscopy

Intravital microscopy

Image acquisitions was done using an upright spinning-disk confocal microscope (DM6 FS; Leica) equipped with a motorized stage (Z Deck; Prior Scientific). The microscope is fitted with a motorized objective turret equipped with 5×/0.15 HCX PL Fluotar, 25×/0.95 HC Fluotar and 40×/1.10 HC PL APO objective lenses (Leica), mounted on an optical table to minimize vibration and totally enclosed in a biosafety cabinet (Noroit). The microscope is coupled to a CSU-W1 confocal head (Yokogawa Electric Corporation) modified with Borealis technology (Oxford Instruments). Four laser excitation wavelengths (488, 561, 642, and 730 nm) were used and visualized with the appropriate band-pass and long-pass filters. Fluorescence signals were detected using 2 sCMOS 2048 × 2048 pixels cameras (Orca Flash v2+, Hamamatsu) allowing simultaneous dual colors imaging. Metamorph acquisition software (Molecular devices) was used to drive the confocal microscope and images were exported as .tiff files.

Widefield time-lapse microscopy

For velocity measurements and actin imaging, migrating cells were recorded for 4-6 hours with a DMi8 (Leica) or IX-83 (Evident) inverted microscopes equipped with controlled atmosphere (37°C, 5% CO_2) using a ×20 dry objective (NA 0.80). One image every 30 s was recorded unless otherwise indicated.

Spinning-disk time-lapse microscopy

For MyosinII-GFP imaging, migrating cells were recorded using a spinning-disk confocal microscope with a Yokogawa CSU-X1 spinning-disc head on a DMI-8 Leica inverted microscope equipped with a Hamamatsu OrcaFlash 4.0 Camera, a NanoScanZ piezo focusing stage (Prior Scientific) and a motorized scanning stage (Marzhauser). One slice with focus on the middle cell cross section was recorded every 5 or 10 s for 1 hour. The spinning-disk microscope was controlled by MetaMorph software (Molecular Devices) and equipped with an incubation chamber that maintained the temperature at 37°C and CO2 concentration at 5%.

For microscopy of Rho/Rac biosensors, and atomic force microscopy (AFM), please refer to the Supplementary Materials for further information

Drugs and dyes

For visualization of the nucleus, microtubules and intracellular calcium in live cells, and for further information about the compounds used in this work, please refer to the Supplementary Materials.

Image analysis

Instantaneous and mean speed, AR and signal localisation

Three single-cell parameters (cell AR, cell speed, and F-actin intracellular distribution) were analyzed using in-house macros in ImageJ/Fiji software (*75*). Briefly, kymographs for each microchannel (in each field of view) were generated using a semi-automated ImageJ macro. Individual cells migrating within the microchannels were segmented on each kymograph using a pixel classification algorithm (Labkit) (*76*), applied to the LifeAct-EGFP or MyoII-EGFP signal to obtain a mask of the entire cell. The cell AR, used as a measure of cell deformation/elongation (Viridis LUT), was computed with Fiji as the ratio of the major axis to the minor axis of the Feret ellipse approximating the cell. For nucleus AR, we used Hoechst signal for segmentation.

Instantaneous cell speed was determined by measuring the displacement of the cell centroid along the microchannel axis between two frames. The back-to-front actin ratio (BFAR) was calculated to evaluate intracellular F-actin distribution. The BFAR corresponds to the ratio of the mean F-actin fluorescence intensity measured in the rear half of the cell mask to that measured in the front half. A BFAR greater than 1 indicates an enrichment of F-actin at the rear of the cell, while a BFAR less than 1 indicates an enrichment of F-actin at the front of the cell. For Rho activity, we defined back region as 15 % of cell rear enrichment and for Rac activity, we used the 25 % of cell front. For MyoII cortical measurements, the whole cell body was first segmented based on the MyoII–GFP signal using the Labkit plugin in Fiji software. The cortical region was defined as a two-pixel-wide band along the cell boundary, corresponding to a width of 0.25 µm. Back cortical MyoII enrichment was then quantified as the ratio of the mean fluorescence intensity measured in the rear 25% of the cell length to that measured in the front 75%.

Spatial analysis of single-cell parameters

The relative speed of cells migrating in microchannels with sharp transitions was calculated for each cell as the ratio of its instantaneous velocity to its average velocity in the first section of the microchannel. In microchannels with successive transitions, the average velocity of each cell was calculated in the first 6 µm section. In microchannels with a gradual narrowing, the relative speed of each cell was computed as the ratio of its instantaneous velocity to its average velocity.

To assess the evolution of BFAR, AR and speed along the *x*-axis of the microchannels, we partitioned the *x*-axis into fixed-size bins. Then, the average across cells in each bin was calculated. To avoid sampling bias and underrepresentation of the fastest cells, we partitioned the *x*-axis into

bins with a length equal to the largest cell displacement measured in the experiment. By doing so, each bin contains at least one measure for each cell. When more than one measure for a cell was recorded in a specific bin, these measures were averaged before the averaging across the cell population. When indicated, relative speed data and BFAR data were log2 transformed prior to the averaging across the cell population. For graphical representation, the evolution of the mean and standard deviation of different parameters (cell speed, aspect ratio, or BFAR) was plotted as a function of *x*-position. Position 0 corresponds to the necking region (sharp transition). Bin size is indicated by the bar length (upper left), and the sliding window is represented by the shift between two consecutive bars. When shown at the bottom, graphs represent the evolution of the fraction of cells displaying changes in parameter values as a function of *x*-position. Speed decrease, increase, or maintenance were defined as fold changes < 0.8, > 1.2, or between 0.8 and 1.2, respectively.

The crossing time between two microchannels sections was calculated as the time between the first cell contact with the narrowing section of the microchannel, and the time at which the whole cell was in the confined section.

Signal density maps

Lifeact-EGFP and Rho biosensor density maps were generated as described (*49*). Briefly, individual neutrophils migrating in microchannels were cropped using the ImageJ software. To map the Lifeact-GFP or Rho signals, images of all timepoints of each individual cell were aligned in a single column. Cell size normalization was applied to each time point according to the mean cell size. To obtain the mean Lifeact-EGFP or Rho biosensor distribution of each cell, an average projection was performed on the *t*-stack. All cell average projections were then size-normalized and averaged to obtain the mean signal distribution of each condition.

Immunostaining, Immunoblots and Flow cytometry

For pMLC2, Lamin A/C immunostainings, cPLA2 immunoblot and flow cytometry analysis of mNeu phenotype, please refer to the Supplementary Materials for further information.

Statistical analysis

As reported in figure legends, two-tailed, Mann-Whitney U test, Kruskal-Wallis test, Wilcoxon rank test, or Spearman correlation was used to determine statistical significance using Prism 10 (GraphPad). Significance was set at $P < 0.05$ and P-values are indicated in figures. For correlation tests, correlation coefficient r are indicated. Dot plots indicate all individual values and line indicate median. When present, larger dots indicate median or mean of independent experiment (biological replicate) and are paired between conditions of the same replicate.

Supplementary Materials

Supplementary Text

Figs. S1 to S5

Table S1

Movies S1 to S21

Data files S1 to S3

MDAR Reproducibility checklist

REFERENCES AND NOTES

1. T. Lämmermann, P. V. Afonso, B. R. Angermann, J. M. Wang, W. Kastenmüller, C. A. Parent, R. N. Germain, Neutrophil swarms require LTB4 and integrins at sites of cell death in vivo. *Nature* 498, 371–375 (2013).
2. S. Nourshargh, P. L. Hordijk, M. Sixt, Breaching multiple barriers: leukocyte motility through venular walls and the interstitium. *Nat. Rev. Mol. Cell Biol.* 11, 366–378 (2010).
3. E. Kolaczkowska, P. Kubes, Neutrophil recruitment and function in health and inflammation. *Nat. Rev. Immunol.* 13, 159–175 (2013).
4. K. A. Brown, S. D. Brain, J. D. Pearson, J. D. Edgeworth, S. M. Lewis, D. F. Treacher, Neutrophils in development of multiple organ failure in sepsis. *The Lancet* 368, 157–169 (2006).
5. S. L. Maas, O. Soehnlein, J. R. Viola, Organ-Specific Mechanisms of Transendothelial Neutrophil Migration in the Lung, Liver, Kidney, and Aorta. *Front. Immunol.* 9, 2739 (2018).
6. C. M. Doerschuk, Mechanisms of Leukocyte Sequestration in Inflamed Lungs. *Microcirculation* 8, 71–88 (2001).
7. M. G. Harding, K. Zhang, J. Conly, P. Kubes, Neutrophil Crawling in Capillaries; A Novel Immune Response to Staphylococcus aureus. *PLoS Pathog.* 10, e1004379 (2014).
8. X. Wang, M. Hossain, A. Bogoslowski, P. Kubes, D. Irimia, Chemotaxing neutrophils enter alternate branches at capillary bifurcations. *Nat. Commun.* 11, 2385 (2020).
9. A. Bogoslowski, E. C. Butcher, P. Kubes, Neutrophils recruited through high endothelial venules of the lymph nodes via PNAd intercept disseminating *Staphylococcus aureus*. *Proc. Natl. Acad. Sci.* 115, 2449–2454 (2018).
10. L. Aoun, P. Nègre, C. Gonsales, V. Seveau De Noray, S. Brustlein, M. Biarnes-Pelicot, M.-P. Valignat, O. Theodoly, Leukocyte transmigration and longitudinal forward-thrusting force in a microfluidic Transwell device. *Biophys. J.* 120, 2205–2221 (2021).
11. K. Wolf, M. Te Lindert, M. Krause, S. Alexander, J. Te Riet, A. L. Willis, R. M. Hoffman, C. G. Figdor, S. J. Weiss, P. Friedl, Physical limits of cell migration: Control by ECM space and nuclear deformation and tuning by proteolysis and traction force. *J. Cell Biol.* 201, 1069–1084 (2013).
12. P. M. Davidson, C. Denais, M. C. Bakshi, J. Lammerding, Nuclear Deformability Constitutes a Rate-Limiting Step During Cell Migration in 3-D Environments. *Cell. Mol. Bioeng.* 7, 293–306 (2014).
13. R. Sakamoto, Z. Izri, Y. Shimamoto, M. Miyazaki, Y. T. Maeda, Geometric trade-off between contractile force and viscous drag determines the actomyosin-based motility of a cell-sized droplet. *Proc. Natl. Acad. Sci.* 119, e2121147119 (2022).
14. J. C. Cruz Hernández, O. Bracko, C. J. Kersbergen, V. Muse, M. Haft-Javaherian, M. Berg, L. Park, L. K. Vinarcsik, I. Ivasyk, D. A. Rivera, Y. Kang, M. Cortes-Canteli, M. Peyrounette, V. Doyeux, A. Smith, J. Zhou, G. Otte, J. D. Beverly, E. Davenport, Y. Davit, C. P. Lin, S. Strickland, C. Iadecola, S. Lorthois, N. Nishimura, C. B. Schaffer, Neutrophil adhesion in brain capillaries reduces cortical blood flow and impairs memory function in Alzheimer's disease mouse models. *Nat. Neurosci.* 22, 413–420 (2019).
15. Ş. E. Erdener, J. Tang, K. Kılıç, D. Postnov, J. T. Giblin, S. Kura, I. A. Chen, T. Vayisoğlu, S. Sakadžić, C. B. Schaffer, D. A. Boas, Dynamic capillary stalls in reperfused ischemic penumbra

contribute to injury: A hyperacute role for neutrophils in persistent traffic jams. *J. Cereb. Blood Flow Metab.* 41, 236–252 (2021).

16. M. El Amki, C. Glück, N. Binder, W. Middleham, M. T. Wyss, T. Weiss, H. Meister, A. Luft, M. Weller, B. Weber, S. Wegener, Neutrophils Obstructing Brain Capillaries Are a Major Cause of No-Reflow in Ischemic Stroke. *Cell Rep.* 33, 108260 (2020).

17. H.-K. Lim, S. Bae, K. Han, B.-M. Kang, Y. Jeong, S.-G. Kim, M. Suh, Seizure-induced neutrophil adhesion in brain capillaries leads to a decrease in postictal cerebral blood flow. *iScience* 26, 106655 (2023).

18. Y. Komaru, L. Ning, C. Lama, A. Suresh, E. Kefaloyianni, M. J. Miller, S. Kawana, H. M. Shepherd, W. Li, D. Kreisel, A. Herrlich, Acute kidney injury triggers hypoxemia by lung intravascular neutrophil retention that reduces capillary blood flow. *J. Clin. Invest.* 135, e186705 (2025).

19. H. D. Moreau, C. Blanch-Mercader, R. Attia, M. Maurin, Z. Alraies, D. Sanséau, O. Malbec, M.-G. Delgado, P. Bousso, J.-F. Joanny, R. Voituriez, M. Piel, A.-M. Lennon-Duménil, Macropinocytosis Overcomes Directional Bias in Dendritic Cells Due to Hydraulic Resistance and Facilitates Space Exploration. *Dev. Cell* 49, 171-188.e5 (2019).

20. H. V. Prentice-Mott, C.-H. Chang, L. Mahadevan, T. J. Mitchison, D. Irimia, J. V. Shah, Biased migration of confined neutrophil-like cells in asymmetric hydraulic environments. *Proc. Natl. Acad. Sci.* 110, 21006–21011 (2013).

21. J. Renkawitz, A. Kopf, J. Stopp, I. De Vries, M. K. Driscoll, J. Merrin, R. Hauschild, E. S. Welf, G. Danuser, R. Fiolka, M. Sixt, Nuclear positioning facilitates amoeboid migration along the path of least resistance. *Nature* 568, 546–550 (2019).

22. H. R. Manley, M. C. Keightley, G. J. Lieschke, The Neutrophil Nucleus: An Important Influence on Neutrophil Migration and Function. *Front. Immunol.* 9, 2867 (2018).

23. B. Calì, M. Deygas, F. Munari, E. Marcuzzi, A. Cassará, L. Toffali, M. Vetralla, M. Bernard, M. Piel, O. Gagliano, M. Mastrogiovanni, C. Laudanna, N. Elvassore, B. Molon, P. Vargas, A. Viola, Atypical CXCL12 signaling enhances neutrophil migration by modulating nuclear deformability. *Sci. Signal.* 15, eabk2552 (2022).

24. S. Sormendi, M. Deygas, A. Sinha, M. Bernard, A. Krüger, I. Kourtzelis, G. Le Lay, P. J. Sáez, M. Gerlach, K. Franke, A. Meneses, M. Kräter, A. Palladini, J. Guck, Ü. Coskun, T. Chavakis, P. Vargas, B. Wielockx, HIF2α is a direct regulator of neutrophil motility. *Blood* 137, 3416–3427 (2021).

25. G. Fossati, I. Mazzucchelli, D. Gritti, G. Ricevuti, S. W. Edwards, D. A. Moulding, M. L. Rossi, In vitro effects of GM-CSF on mature peripheral blood neutrophils. *Int. J. Mol. Med.* 1, 943–951 (1998).

26. P. Friedl, K. Wolf, J. Lammerding, Nuclear mechanics during cell migration. *Curr. Opin. Cell Biol.* 23, 55–64 (2011).

27. A. J. Lomakin, C. J. Cattin, D. Cuvelier, Z. Alraies, M. Molina, G. P. F. Nader, N. Srivastava, P. J. Sáez, J. M. Garcia-Arcos, I. Y. Zhitnyak, A. Bhargava, M. K. Driscoll, E. S. Welf, R. Fiolka, R. J. Petrie, N. S. De Silva, J. M. González-Granado, N. Manel, A. M. Lennon-Duménil, D. J. Müller, M. Piel, The nucleus acts as a ruler tailoring cell responses to spatial constraints. *Science* 370, eaba2894 (2020).

28. V. Venturini, F. Pezzano, F. C. Castro, H.-M. Häkkinen, S. Jiménez-Delgado, M. Colomer-Rosell, M. Marro, Q. Tolosa-Ramon, S. Paz-López, M. A. Valverde, J. Weghuber, P. Loza-Alvarez, M. Krieg, S. Wieser, V. Ruprecht, The nucleus measures shape changes for cellular proprioception to control dynamic cell behavior. *Science* 370, eaba2644 (2020).

29. S. B. Arya, F. Jordan-Javed, K. Loesel, Y. Choi, S. P. Collie, L. E. Hein, B. M. Baker, E. Yoon, C. A. Parent, cPLA2α targeting to exosomes connects nuclear deformation to LTB4-signaling during neutrophil chemotaxis. *Sci. Adv.* 12, eaea2784 (2026).

30. H. R. Manley, M. C. Keightley, G. J. Lieschke, The Neutrophil Nucleus: An Important Influence on Neutrophil Migration and Function. *Front. Immunol.* 9 (2018).

31. E. Van Grinsven, A. K. Mukherjee, I. A. Udalova, Shaping neutrophil morphology and function: the importance of a segmented nucleus. *Nat. Rev. Immunol.*, doi: 10.1038/s41577-025-01237-3 (2025).

32. A. C. Rowat, D. E. Jaalouk, M. Zwerger, W. L. Ung, I. A. Eydelnant, D. E. Olins, A. L. Olins, H. Herrmann, D. A. Weitz, J. Lammerding, Nuclear Envelope Composition Determines the Ability of Neutrophil-type Cells to Passage through Micron-scale Constrictions. *J. Biol. Chem.* 288, 8610–8618 (2013).

33. E. M. Balzer, Z. Tong, C. D. Paul, W. Hung, K. M. Stroka, A. E. Boggs, S. S. Martin, K. Konstantopoulos, Physical confinement alters tumor cell adhesion and migration phenotypes. *FASEB J.* 26, 4045–4056 (2012).

34. Y.-J. Liu, M. Le Berre, F. Lautenschlaeger, P. Maiuri, A. Callan-Jones, M. Heuzé, T. Takaki, R. Voituriez, M. Piel, Confinement and Low Adhesion Induce Fast Amoeboid Migration of Slow Mesenchymal Cells. *Cell* 160, 659–672 (2015).

35. F. Amiri, A. A. Akinpelu, W. C. Keith, F. Hemmati, R. S. Vaghasiya, D. Bowen, R. S. Waliagha, C. Wang, P. Chen, A. K. Mitra, Y. Li, P. Mistriotis, Confinement controls the directional cell responses to fluid forces. *Cell Rep.* 43, 114692 (2024).

36. N. Nakazawa, G. Grenci, Y. Kameo, N. Takeda, T. Sawada, J. Kurisu, Z. Zhang, K. Toma, T. Adachi, K. Nonomura, M. Kengaku, PIEZO1-dependent mode switch of neuronal migration in heterogeneous microenvironments in the developing brain. *Cell Rep.* 44, 115405 (2025).

37. W.-C. Hung, J. R. Yang, C. L. Yankaskas, B. S. Wong, P.-H. Wu, C. Pardo-Pastor, S. A. Serra, M.-J. Chiang, Z. Gu, D. Wirtz, M. A. Valverde, J. T. Yang, J. Zhang, K. Konstantopoulos, Confinement Sensing and Signal Optimization via Piezo1/PKA and Myosin II Pathways. *Cell Rep.* 15, 1430–1441 (2016).

38. K. Wilson, A. Lewalle, M. Fritzsche, R. Thorogate, T. Duke, G. Charras, Mechanisms of leading edge protrusion in interstitial migration. *Nat. Commun.* 4, 2896 (2013).

39. B. McDonald, E. F. McAvoy, F. Lam, V. Gill, C. De La Motte, R. C. Savani, P. Kubes, Interaction of CD44 and hyaluronan is the dominant mechanism for neutrophil sequestration in inflamed liver sinusoids. *J. Exp. Med.* 205, 915–927 (2008).

40. M. A. Quintanilla, J. A. Hammer, J. R. Beach, Non-muscle myosin 2 at a glance. *J. Cell Sci.* 136, jcs260890 (2023).

41. P. Maiuri, J.-F. Rupprecht, S. Wieser, V. Ruprecht, O. Bénichou, N. Carpi, M. Coppey, S. De Beco, N. Gov, C.-P. Heisenberg, C. Lage Crespo, F. Lautenschlaeger, M. Le Berre, A.-M. Lennon-Dumenil, M. Raab, H.-R. Thiam, M. Piel, M. Sixt, R. Voituriez, Actin Flows Mediate a Universal Coupling between Cell Speed and Cell Persistence. *Cell* 161, 374–386 (2015).

42. A. Georgantzoglou, H. Poplimont, H. A. Walker, T. Lämmermann, M. Sarris, A two-step search and run response to gradients shapes leukocyte navigation in vivo. *J. Cell Biol.* 221, e202103207 (2022).

43. Y. Zhang, M. A. Conti, D. Malide, F. Dong, A. Wang, Y. A. Shmist, C. Liu, P. Zerfas, M. P. Daniels, C.-C. Chan, E. Kozin, B. Kachar, M. J. Kelley, J. B. Kopp, R. S. Adelstein, Mouse

models of MYH9-related disease: mutations in nonmuscle myosin II-A. *Blood* 119, 238–250 (2012).

44. H. De Belly, A. F. Gallen, E. Strickland, D. C. Estrada, P. J. Zager, T. L. Nagy, J. K. Burkhardt, H. Turlier, O. D. Weiner, Long range mutual activation establishes Rho and Rac polarity during cell migration. *BioRxiv Prepr. Serv. Biol.*, 2024.10.01.616161 (2025).

45. A. Diz-Muñoz, K. Thurley, S. Chintamen, S. J. Altschuler, L. F. Wu, D. A. Fletcher, O. D. Weiner, Membrane Tension Acts Through PLD2 and mTORC2 to Limit Actin Network Assembly During Neutrophil Migration. *PLOS Biol.* 14, e1002474 (2016).

46. S. K. Yadav, S. W. Feigelson, F. Roncato, M. Antman-Passig, O. Shefi, J. Lammerding, R. Alon, Frontline Science: Elevated nuclear lamin A is permissive for granulocyte transendothelial migration but not for motility through collagen I barriers. *J. Leukoc. Biol.* 104, 239–251 (2018).

47. B. McKee, S. Abolghasemzade, T.-C. Wang, K. Harsh, S. Kaur, R. Blanchard, K. B. Menon, M. Mohajeri, R. B. Dickinson, T. P. Lele, Excess surface area of the nuclear lamina enables unhindered cell migration through constrictions. *Sci. Adv.* 11, eads6573 (2025).

48. T. Y.-C. Tsai, S. R. Collins, C. K. Chan, A. Hadjitheodorou, P.-Y. Lam, S. S. Lou, H. W. Yang, J. Jorgensen, F. Ellett, D. Irimia, M. W. Davidson, R. S. Fischer, A. Huttenlocher, T. Meyer, J. E. Ferrell, J. A. Theriot, Efficient Front-Rear Coupling in Neutrophil Chemotaxis by Dynamic Myosin II Localization. *Dev. Cell* 49, 189-205.e6 (2019).

49. P. Vargas, P. Maiuri, M. Bretou, P. J. Sáez, P. Pierobon, M. Maurin, M. Chabaud, D. Lankar, D. Obino, E. Terriac, M. Raab, H.-R. Thiam, T. Brocker, S. M. Kitchen-Goosen, A. S. Alberts, P. Sunareni, S. Xia, R. Li, R. Voituriez, M. Piel, A.-M. Lennon-Duménil, Innate control of actin nucleation determines two distinct migration behaviours in dendritic cells. *Nat. Cell Biol.* 18, 43–53 (2016).

50. S. K. Yoo, Q. Deng, P. J. Cavnar, Y. I. Wu, K. M. Hahn, A. Huttenlocher, Differential Regulation of Protrusion and Polarity by PI(3)K during Neutrophil Motility in Live Zebrafish. *Dev. Cell* 18, 226–236 (2010).

51. A. Leithner, A. Eichner, J. Müller, A. Reversat, M. Brown, J. Schwarz, J. Merrin, D. J. J. de Gorter, F. Schur, J. Bayerl, I. de Vries, S. Wieser, R. Hauschild, F. P. L. Lai, M. Moser, D. Kerjaschki, K. Rottner, J. V. Small, T. E. B. Stradal, M. Sixt, Diversified actin protrusions promote environmental exploration but are dispensable for locomotion of leukocytes. *Nat. Cell Biol.* 18, 1253–1259 (2016).

52. M. Chabaud, M. L. Heuzé, M. Bretou, P. Vargas, P. Maiuri, P. Solanes, M. Maurin, E. Terriac, M. L. Berre, D. Lankar, T. Piolot, R. S. Adelstein, Y. Zhang, M. Sixt, J. Jacobelli, O. Bénichou, R. Voituriez, M. Piel, A.-M. Lennon-Duménil, Cell migration and antigen capture are antagonistic processes coupled by myosin II in dendritic cells. *Nat. Commun.* 6, 7526 (2015).

53. M. Bretou, P. J. Sáez, D. Sanséau, M. Maurin, D. Lankar, M. Chabaud, C. Spampanato, O. Malbec, L. Barbier, S. Muallem, P. Maiuri, A. Ballabio, J. Helft, M. Piel, P. Vargas, A.-M. Lennon-Duménil, Lysosome signaling controls the migration of dendritic cells. *Sci. Immunol.* 2, eaak9573 (2017).

54. P. J. Sáez, P. Vargas, K. F. Shoji, P. A. Harcha, A.-M. Lennon-Duménil, J. C. Sáez, ATP promotes the fast migration of dendritic cells through the activity of pannexin 1 channels and P2X7 receptors. *Sci. Signal.* 10, eaah7107 (2017).

55. H. Keller, A. D. Zadeh, P. Eggli, Localised depletion of polymerised actin at the front of Walker carcinosarcoma cells increases the speed of locomotion. *Cell Motil. Cytoskeleton* 53, 189–202 (2002).

56. N. Srivastava, D. Traynor, M. Piel, A. J. Kabla, R. R. Kay, Pressure sensing through Piezo channels controls whether cells migrate with blebs or pseudopods. *Proc. Natl. Acad. Sci.* 117, 2506–2512 (2020).

57. W.-C. Hung, S.-H. Chen, C. D. Paul, K. M. Stroka, Y.-C. Lo, J. T. Yang, K. Konstantopoulos, Distinct signaling mechanisms regulate migration in unconfined versus confined spaces. *J. Cell Biol.* 202, 807–824 (2013).

58. T. Brunet, M. Albert, W. Roman, M. C. Coyle, D. C. Spitzer, N. King, A flagellate-to-amoeboid switch in the closest living relatives of animals. *eLife* 10, e61037 (2021).

59. B. Enyedi, M. Jelcic, P. Niethammer, The Cell Nucleus Serves as a Mechanotransducer of Tissue Damage-Induced Inflammation. *Cell* 165, 1160–1170 (2016).

60. Z. Alraies, C. A. Rivera, M.-G. Delgado, D. Sanséau, M. Maurin, R. Amadio, G. Maria Piperno, G. Dunsmore, A. Yatim, L. Lacerda Mariano, A. Kniazeva, V. Calmettes, P. J. Sáez, A. Williart, H. Popard, M. Gratia, O. Lamiable, A. Moreau, Z. Fusilier, L. Crestey, B. Albaud, P. Legoix, A. S. Dejean, A.-L. Le Dorze, H. Nakano, D. N. Cook, T. Lawrence, N. Manel, F. Benvenuti, F. Ginhoux, H. D. Moreau, G. P. F. Nader, M. Piel, A.-M. Lennon-Duménil, Cell shape sensing licenses dendritic cells for homeostatic migration to lymph nodes. *Nat. Immunol.* 25, 1193–1206 (2024).

61. H. De Belly, S. Yan, H. Borja da Rocha, S. Ichbiah, J. P. Town, P. J. Zager, D. C. Estrada, K. Meyer, H. Turlier, C. Bustamante, O. D. Weiner, Cell protrusions and contractions generate long-range membrane tension propagation. *Cell* 186, 3049-3061.e15 (2023).

62. S. Saha, J. P. Town, O. D. Weiner, Mechanosensitive mTORC2 independently coordinates leading and trailing edge polarity programs during neutrophil migration. *Mol. Biol. Cell* 34, ar35 (2023).

63. C. Shen, A. Cerf, J. Postat, A. Bhagrath, M. Merino, A. Mingarelli, G. Barnes, D. Patel, D. Rogers, V. M. Luo, A. Abu-Thuraia, C. Schneider, D. F. Quail, A. Sharma, W.-K. Suh, A. Ehrlicher, J.-F. Côté, J. N. Mandl, A Dock8-dependent mechanosensitive central actin pool maintains T cell shape and protects the nucleus during migration. *Sci. Immunol.* 10, eadt9239 (2025).

64. P. Reis-Rodrigues, M. J. Avellaneda, N. Canigova, F. Gaertner, K. Vaahtomeri, M. Riedl, I. De Vries, J. Merrin, R. Hauschild, Y. Fukui, A. Juanes Garcia, M. Sixt, Migrating immune cells globally coordinate protrusive forces. *Nat. Immunol.* 26, 1258–1266 (2025).

65. J. Meyers, J. Craig, D. J. Odde, Potential for Control of Signaling Pathways via Cell Size and Shape. *Curr. Biol.* 16, 1685–1693 (2006).

66. E. K. S. Lee, M. R. Gillrie, L. Li, J. W. Arnason, J. H. Kim, L. Babes, Y. Lou, A. Sanati-Nezhad, S. K. Kyei, M. M. Kelly, C. H. Mody, M. Ho, B. G. Yipp, Leukotriene B4-Mediated Neutrophil Recruitment Causes Pulmonary Capillaritis during Lethal Fungal Sepsis. *Cell Host Microbe* 23, 121-133.e4 (2018).

67. N. Ruef, J. Martínez Magdaleno, X. Ficht, V. Purvanov, M. Palayret, S. Wissmann, P. Pfenninger, B. Stolp, F. Thelen, J. Barreto De Albuquerque, P. Germann, J. Sharpe, J. Abe, D. F. Legler, J. V. Stein, Exocrine gland–resident memory CD8 $^{+}$ T cells use mechanosensing for tissue surveillance. *Sci. Immunol.* 8, eadd5724 (2023).

68. J. Riedl, K. C. Flynn, A. Raducanu, F. Gärtner, G. Beck, M. Bösl, F. Bradke, S. Massberg, A. Aszodi, M. Sixt, R. Wedlich-Söldner, Lifeact mice for studying F-actin dynamics. *Nat. Methods* 7, 168–169 (2010).

69. M. Amorós-Pérez, A. Del Monte-Monge, P. Gonzalo, M. J. Andrés-Manzano, C. Rius, V. Fanjul, C. González-Gómez, G. Moreno, A. Benguría, A. Dopazo, F. Sánchez-Cabo, C. Torroja, F.

Martínez De Benito, B. Calì, P. Vargas, C. Silvestre-Roig, J. M. González-Granado, H. Bueno, J. J. Fuster, V. Andrés, Lamin A/C Expression in Hematopoietic Cells Declines During Human Aging and Constrains Atherosclerosis in Mice. *Arterioscler. Thromb. Vasc. Biol.* 45, 1616–1635 (2025).

70. B. E. Clausen, C. Burkhardt, W. Reith, R. Renkawitz, I. Förster, Conditional gene targeting in macrophages and granulocytes using LysMcre mice. *Transgenic Res.* 8, 265–277 (1999).

71. V. Manriquez, P. Nivoit, T. Urbina, H. Echenique-Rivera, K. Melican, M.-P. Fernandez-Gerlinger, P. Flamant, T. Schmitt, P. Bruneval, D. Obino, G. Duménil, Colonization of dermal arterioles by Neisseria meningitidis provides a safe haven from neutrophils. *Nat. Commun.* 12, 4547 (2021).

72. D. Dal-Secco, J. Wang, Z. Zeng, E. Kolaczkowska, C. H. Y. Wong, B. Petri, R. M. Ransohoff, I. F. Charo, C. N. Jenne, P. Kubes, A dynamic spectrum of monocytes arising from the in situ reprogramming of CCR2+ monocytes at a site of sterile injury. *J. Exp. Med.* 212, 447–456 (2015).

73. P. Vargas, E. Terriac, A.-M. Lennon-Duménil, M. Piel, Study of cell migration in microfabricated channels. *J. Vis. Exp. JoVE*, e51099 (2014).

74. M. Wu, F. Xiao, R. M. Johnson-Paben, S. T. Retterer, X. Yin, K. B. Neeves, Single- and two-phase flow in microfluidic porous media analogs based on Voronoi tessellation. *Lab. Chip* 12, 253–261 (2011).

75. J. Schindelin, I. Arganda-Carreras, E. Frise, V. Kaynig, M. Longair, T. Pietzsch, S. Preibisch, C. Rueden, S. Saalfeld, B. Schmid, J.-Y. Tinevez, D. J. White, V. Hartenstein, K. Eliceiri, P. Tomancak, A. Cardona, Fiji: an open-source platform for biological-image analysis. *Nat. Methods* 9, 676–682 (2012).

76. M. Arzt, J. Deschamps, C. Schmied, T. Pietzsch, D. Schmidt, P. Tomancak, R. Haase, F. Jug, LABKIT: Labeling and Segmentation Toolkit for Big Image Data. *Front. Comput. Sci.* 4 (2022).

Acknowledgments: We thank all the volunteers who kindly donated blood samples for our experiments**.** We thank F. Sepulveda (Institut Imagine, Paris, France) for sharing mice stocks. We thank M. Bernard for helping with raw data processing from Metamorph. We thank I. Mikaelian for his valuable feedback. We thank the animal facilities of the Institut Curie and SFR Necker, and the microscopy facilities of IPGG and SFR Necker for equipment and technical assistance.

Funding: this work was supported by The French National Institutes of Health and Medical Research (INSERM). This work received funding of the Agence Nationale pour la Recherche (ANR-16-CE13-0009, ANR-22-CE15-0041, ANR-21-CE17-0050); Labex IPGG; IdEx Université de Paris « Chaires nouvelles équipes » (P.V.). FRM postdoc fellowship (SPF201809007121) (M.D.); Human Frontier Science Program (No. LT000941/2021-C) (T.J.). Labex IBEID (ANR 10-LBX-62 IBEID) (G.D.) and DESTOP ERC Advanced Grant; Fondation ARC pour la recherche sur le cancer (grant ARCDOC42023010006205) (M.B.); FRM team EQU202103012677 (M.P.) and the support of "Institut Pierre-Gilles de Gennes" (laboratoire d'excellence, "Investissements d'avenir" program ANR-10-IDEX-0001-02 PSL and ANR-10-LABX-31), ERC Synergy (101071470–SHAPINCELLFATE) (M.P and AM.L-D). The J.M.G.-G. laboratory is supported by grants PI24/00146, funded by the Instituto de Salud Carlos III (ISCIII) and the European Union, by Comunidad de Madrid, grant number PIPF-2022/SAL-GL-24254 (M.O.-Z.), and by Universidad Francisco de Vitoria (A.S.). Work in the laboratory of V.A. is supported by grant PID2022-141211OB-I00 funded by the Spanish Ministry of Science, Innovation, and

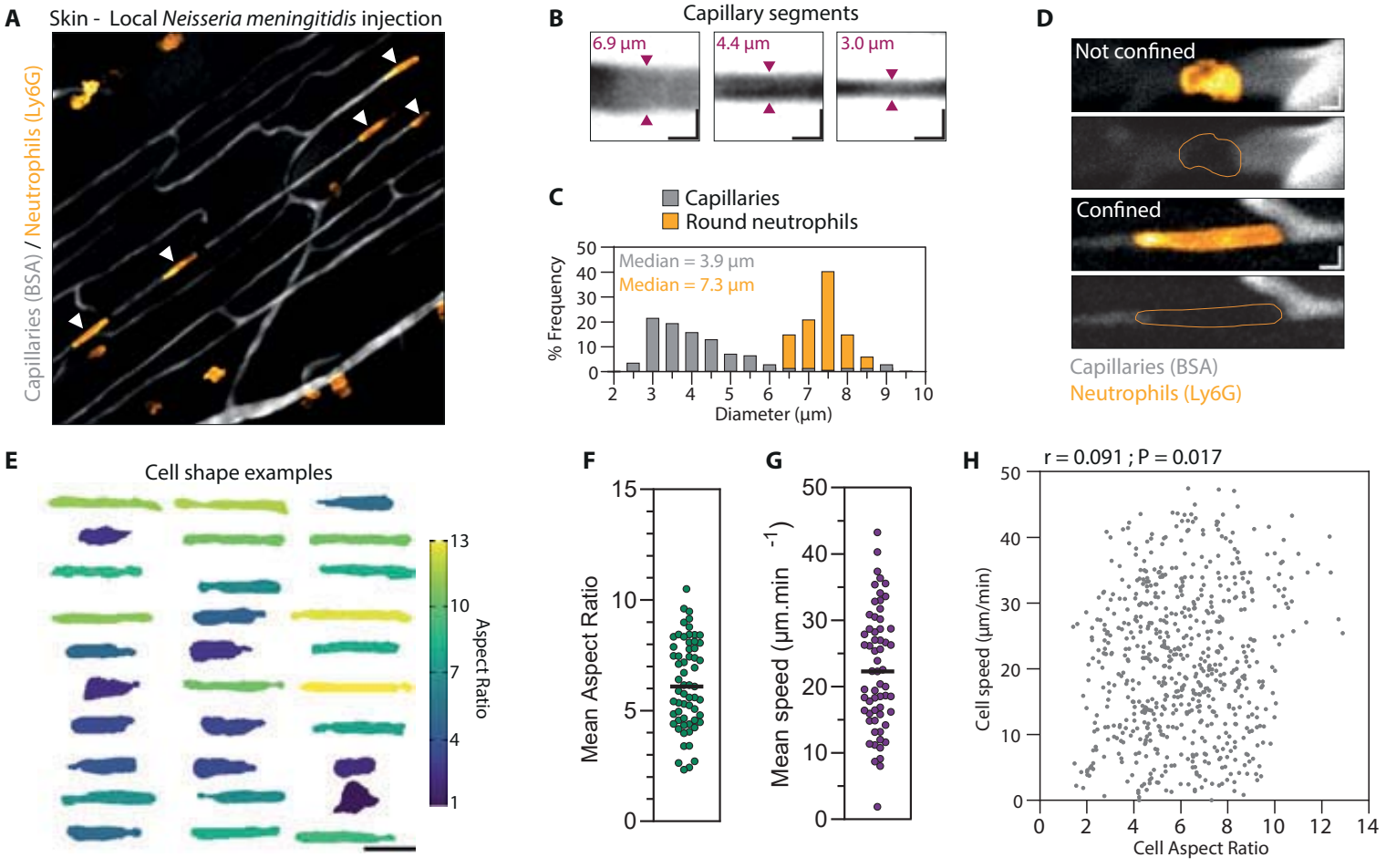
Universities (MICIU) / Agencia Estatal de Investigación (AEI) (MICIU/AEI/10.13039/501100011033) and by the European Regional Development Fund/European Union (ERDF/EU). The CNIC is supported by the ISCIII, the MICIU, and the Pro-CNIC Foundation and is a Severo Ochoa Center of Excellence (grant CEX2020-001041-S funded by MICIU/AEI/10.13039/501100011033). This work was supported by the National Institutes of Health R35GM118167 (O.W) and K99GM154115 (H.D.B)

Author contributions: Conceptualization: M.D., M.P., and P.V. Funding acquisition: G.D., A.M.L.D., J.M.G.G., V.A., O.D.W., M.P., and P.V. Investigation: M.D., M.B., P.N., H.D.B., and L.B. Methodology: E.T., R.A., A.D., T.J., D.C., M.G.G., L.W., M.M., E.T., O.B., A.K., P.G., M.O.Z., A.S., R.G.B., P.G., and S.G. Supervision: G.D., A.M.L.D., O.D.W., M.P., P.V. Visualization: M.D., and M.B. Writing—original draft: M.D., M.P., and P.V. Writing—review and editing: M.D., M.P., and P.V.

Competing interests: Authors declare that they have no competing interests.

Data and materials availability: Uncropped protein immunoblot is provided in data file S1. Tabulated data underlying main and supplementary figures are provided in data file S2 and S3, respectively. All data and materials from this study are available from the corresponding authors upon reasonable request.

Neutrophils in skin capillaries - in vivo



Neutrophils in microchannels - in vitro

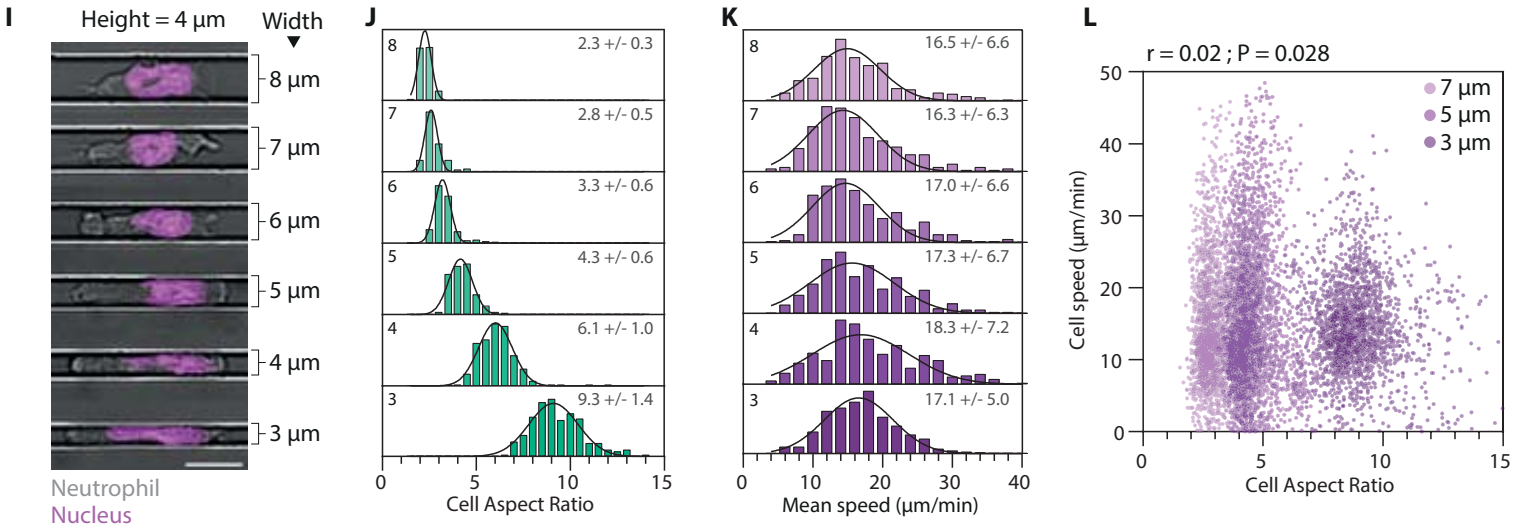


Fig. 1. Neutrophil migration speed in capillaries is independent of confinement strength in vivo and in vitro. (**A** to **H**) Migration and deformation of endogenous murine neutrophils two hours after *N.meningitidis* local skin injection. (A) Spinning disk-confocal images of skin capillaries (A and B) and neutrophils (A, D). Neutrophils inside capillaries are indicated with arrowheads (A). (C) Frequency distribution of the diameter of capillaries (n = 139) and round neutrophils in large vessels (n = 67). (E) Montage of 30 cells pseudo-colored by the value of their aspect ratio (AR). Individual mean cell AR (F), mean cell speed (G), n = 61 cells. (H) Scatter plot comparing instantaneous speed and instantaneous cell AR, n = 679 timepoints from 61 cells. (**I** to **L**) Mature mouse neutrophils (mNeu) migrating in microchannels of different widths. Representative widefield microscopy images of individual mNeu (Hoechst, magenta) in each channel size (I). Distribution of mean cell AR (J), n > 150 cells per channel size; and mean cell speed (K), n > 250 cells per channel size. Scatter plot comparing instantaneous speed and instantaneous cell AR of mNeu in 7, 5 and 3 µm channel width (L). Data are one representative of three independent experiments, n = 2189 (7 µm), n = 2876 (n = 5 µm), n = 2137 (3 µm). Data are pooled from three [(C), (F), (G), (H)] or five (K) independent experiments. Data are displayed as median by a line [(F) and (G)], or frequency distributions (percentage) with indicated means ± SD [(C), (J), (K)]. Each dot represents [(F), (G), (H), (L)] one cell. Data were analyzed by [(H) and (L)] Spearman correlation test (two-tailed). ns, not significant. Scale bar: 5 µm [(B), (D), (I)], 10 µm (E), 20 µm (A).

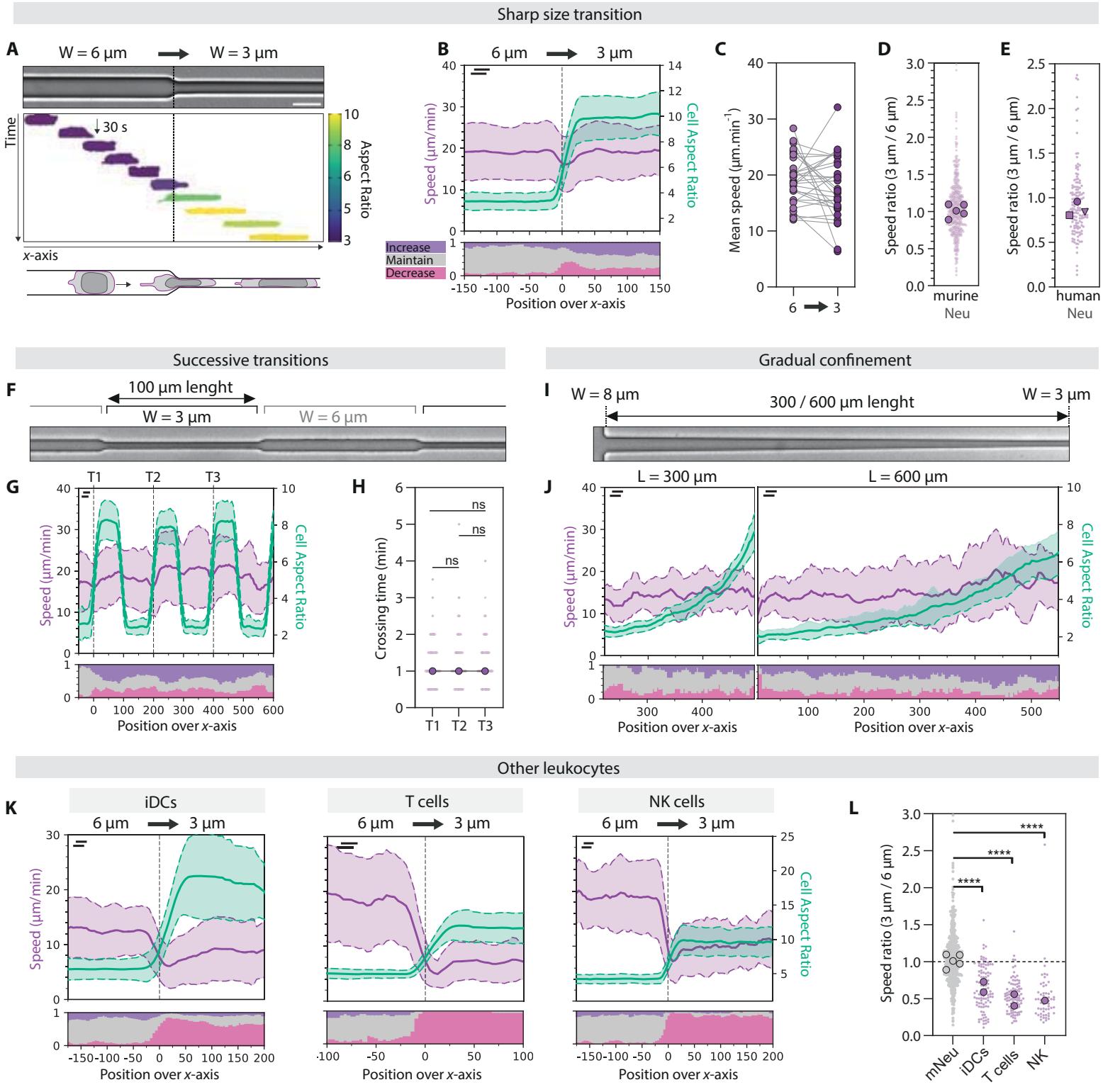

Sharp size transition
A
W = 6 µm
W = 3 µm
Time
30 s
x-axis
Aspect Ratio
B
6 µm
3 µm
Speed (µm/min)
Cell Aspect Ratio
Increase
Maintain
Decrease
Position over x-axis
C
Mean speed (µm.min-1)
6
3
D
Speed ratio (3 µm / 6 µm)
murine
Neu
E
human
Neu
Successive transitions
F
100 µm lenght
W = 3 µm
W = 6 µm
G
T1
T2
T3
Speed (µm/min)
Cell Aspect Ratio
Position over x-axis
H
Crossing time (min)
ns
Gradual confinement
I
W = 8 µm
300 / 600 µm lenght
W = 3 µm
J
L = 300 µm
L = 600 µm
Speed (µm/min)
Cell Aspect Ratio
Position over x-axis
Other leukocytes
K
iDCs
T cells
NK cells
6 µm
3 µm
Speed (µm/min)
Cell Aspect Ratio
Position over x-axis
L
Speed ratio (3 µm / 6 µm)
****
mNeu
iDCs
T cells
NK

Fig. 2. Neutrophils maintain migration speed across dynamic changes in confinement. (**A** to **E**) Migration of neutrophil in size-transition microchannels narrowing from 6 µm to 3 µm width (4 µm height). Kimograph showing mouse neutrophil (mNeu) aspect ratio (AR) transition (A). mNeu Speed and AR evolution (B), N = 122 cells. Average speeds of 30 mNeu (C). mNeu speed ratios: ratio of the mean speed in the 3 µm section normalized by the mean speed in the 6 µm section, n = 544 cells (D). Human primary neutrophil (hNeu) speed ratios, n = 144 cells (E). (**F** to **H**) Migration of mNeu in microchannels with successive transitions between 6 µm and 3 µm width. Image and dimensions of a microchannel (F). Mean speed, n = 90 cells (G). Crossing time (H) for three consecutive transitions. N > 100 cells for each transition. (**I** and **J**) Migration of mNeu funnel-shaped microchannel with gradual confinement from 8 µm to 3 µm width. Image of a microchannel (I). Average speed (J) in 300 µm (n = 21 cells) and 600 µm length (n = 23 cells). (**K** and **L**) Migration of immature dendritic cells (iDCs), T cells and NK cells in a size-transition microchannel. Average speed and AR (K), n = 79 iDCs; n = 38 T cells and n = 56 NK cells. Speed ratios (L), n = 103 iDCs; n = 96 T cells; n = 58 NK cells. Data are one representative of five (B), three [(J) 600 µm], two [(G), (H), (J) 300 µm, (K) iDCs and T cells] and one experiment [(K) NK cells]. Data are pooled from five (D), three (E), two [(L) iDCs, T cells]. Data were analyzed by (H) Wilcoxon test, or (L) Mann Whitney test. ns, not significant, ****P < 0.0001.

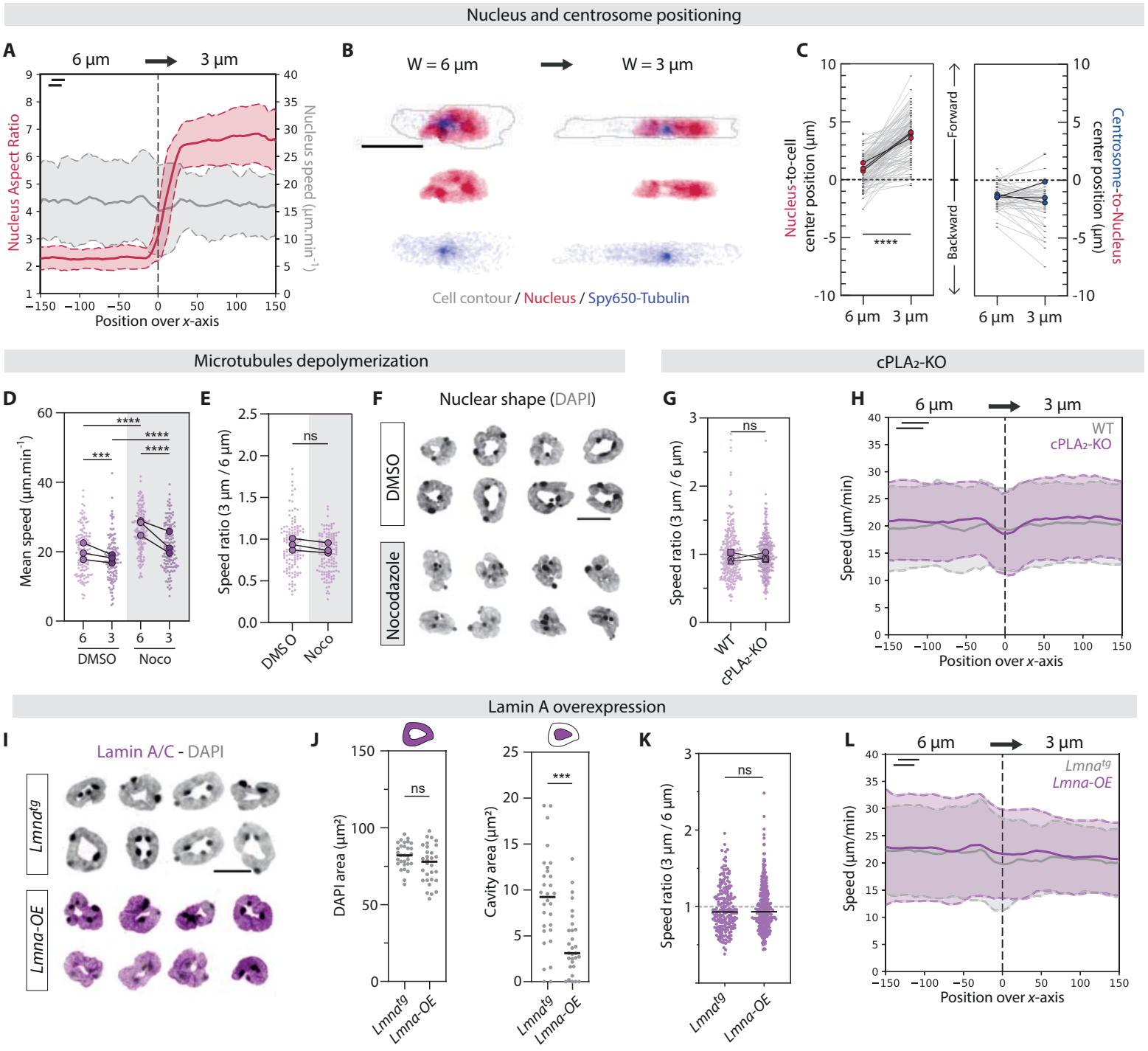

Nucleus and centrosome positioning
A
6 µm
3 µm
Nucleus Aspect Ratio
Nucleus speed (µm.min⁻¹)
Position over x-axis
B
W = 6 µm
W = 3 µm
Cell contour / Nucleus / Spy650-Tubulin
C
Nucleus-to-cell center position (µm)
Centrosome-to-Nucleus center position (µm)
Forward
Backward
****
6 µm
3 µm
Microtubules depolymerization
D
Mean speed (µm.min⁻¹)
DMSO
Noco
E
Speed ratio (3 µm / 6 µm)
ns
F
Nuclear shape (DAPI)
DMSO
Nocodazole
cPLA2-KO
G
Speed ratio (3 µm / 6 µm)
WT
cPLA2-KO
H
WT
cPLA2-KO
Speed (µm/min)
Position over x-axis
Lamin A overexpression
I
Lamin A/C - DAPI
Lmna^tg
Lmna-OE
J
DAPI area (µm²)
Cavity area (µm²)
***
K
Speed ratio (3 µm / 6 µm)
L
Lmna^tg
Lmna-OE
Speed (µm/min)
Position over x-axis

Fig. 3. Role of nuclear properties and microtubules on mNeu migration. (**A** to **C**) Migration of mNeu in size-transition microchannels narrowing from 6 µm to 3 µm width. (A) Evolution of nucleus speed (gray) and nucleus aspect ratio (Red) over the *x*-position; n = 50 cells. (B) Cell contour (gray), nucleus (red) and microtubules (blue) of one mNeu. (C) Nucleus-to-cell center position (left) and centrosome-to-nucleus center position (right), n = 121 cells (left), n = 53 cells (right). (**D** to **F**) Effect of Nocodazole (Noco) on mean speed (D), speed ratio (E) of mNeu migrating from 6 µm to 3 µm width section, and on mNeu nuclear shape fixed on glass coverslip (F). n = 128 (DMSO) and 133 (Noco) cells. (**G** and **H**) Migration of WT and $cPLA_2$-KO mNeu in size-transition channel. Speed ratio (G), n =287 (WT) and n = 342 ($cPLA_2$-KO) cells. (H) Evolution of speed over the *x*-position mNeu, n > 110 cells for each condition. (**I** and **J**) Lamin A/C immunostaining (I) and nuclear morphology (J) of mNeu from *Lmna*^{tg} mice (control) and LysM-Cre; Tg-*Lmna* mice (*Lmna-OE*, Lamin A overexpression), n = 30 cells. (**K** and **L**) Migration of control and Lamin A overexpressing mNeu in size-transition channel. Speed ratios (K), n = 204 (*Lmna*^{tg}) and n = 342 (*Lmna-OE*) cells. (L) Evolution of speed over the *x*-position, n = 81 (*Lmna*^{tg}) and n = 216 (*Lmna-OE*) cells. Data are pooled from three [(C), (D), (E), (G), (K) *Lmna-OE*] or two [(K) *Lmna*^{tg})] independent experiments. Data are one representative [(A), (H), (J), (L)] of two or three independent experiments. Data were analyzed by [(D), (E), (G)] Wilcoxon test, or [(C), (D), (J), (K)] Mann Whitney test. ns, not significant, ***P < 0.001, ****P < 0.0001. Scale bar: 10 µm.

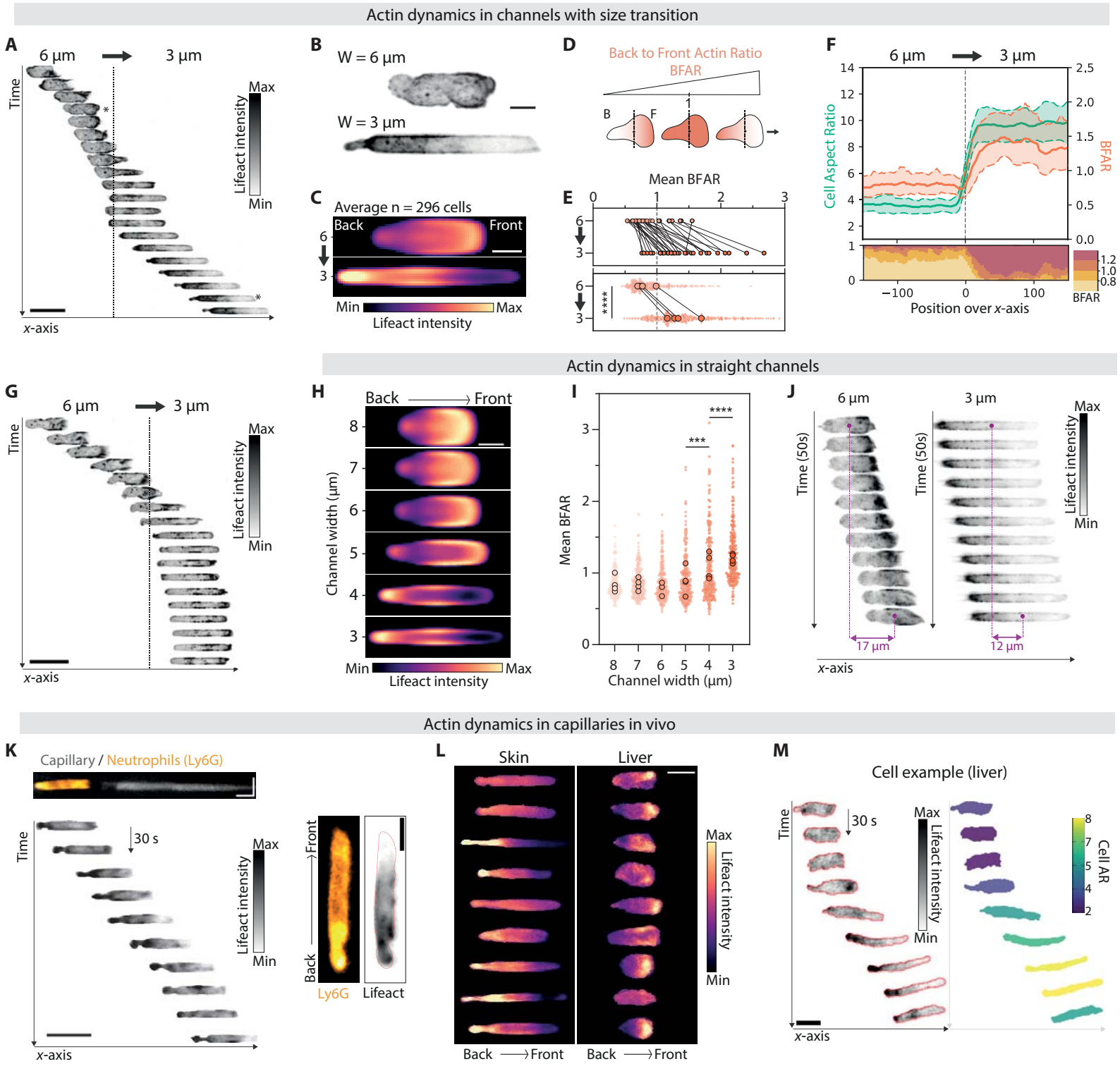

Actin dynamics in channels with size transition
A
6 µm
3 µm
Time
Max
Lifeact intensity
Min
x-axis
B
W = 6 µm
W = 3 µm
C
Average n = 296 cells
Back
Front
Min
Max
Lifeact intensity
D
Back to Front Actin Ratio
BFAR
B
F
E
Mean BFAR
****
F
6 µm
3 µm
Cell Aspect Ratio
BFAR
Position over x-axis
Actin dynamics in straight channels
G
6 µm
3 µm
Time
Max
Lifeact intensity
Min
x-axis
H
Back
Front
Channel width (µm)
Min
Max
Lifeact intensity
I
Mean BFAR
***
****
Channel width (µm)
J
6 µm
3 µm
Time (50s)
Max
Lifeact intensity
Min
17 µm
12 µm
x-axis
Actin dynamics in capillaries in vivo
K
Capillary / Neutrophils (Ly6G)
Time
30 s
Max
Lifeact intensity
Min
x-axis
Front
Back
Ly6G
Lifeact
L
Skin
Liver
Max
Lifeact intensity
Min
Back
Front
M
Cell example (liver)
Time
30 s
Max
Lifeact intensity
Min
Cell AR
x-axis

Fig. 4. Neutrophil F-actin polarity is regulated by confinement strength. (**A** to **G**) Migration of Lifeact-EGFP expressing mNeu in size-transition microchannel. (A) Kimograph showing Lifeact-EGFP intensity in gray. (B) Magnification of the cell in 6 µm and 3 µm width section at timepoints indicated by * in (A). (C) Average mapping of Lifeact-EGFP intensity, n = 348 cells. (D) Schematic representation of Back to Front Actin Ratio (BFAR). (E) Mean BFAR of n = 30 cells (top) and n = 348 cells (Bottom). (F) Evolution of BFAR and cell AR over the *x*-axis, n = 50 cells. (G) Kimograph of a cell slowing down at the transition. (**H** to **J**) Migration of Lifeact-EGFP expressing mNeu in straight microchannels of 8-to-3 µm widths. Average mapping of Lifeact-EGFP intensity (H) and mean BFAR (I), n > 200 cells per channel width. (J) Kimographs of cell in 6 µm and 3 µm width channels. (**K** to **M**) Migration of Lifeact-EGFP expressing mNeu in skin capillaries and liver sinusoids. (K) Kimograph showing a cell (stained with anti-Ly6G) confined in a skin capillary. (L) Average Lifeact-EGFP intensity mapping of nine cells migrating in confined skin capillaries (left) or large liver sinusoids (right). (M) Kimograph showing actin dynamics (left) and cell deformation (aspect ratio, right) in liver sinusoid. Each dot represents one cell and large dots represent the median of each experiment [(E), (I)]. Data are pooled from four [(C), (E), (I)]. Data are one representative of four experiments (F). Data were analyzed by (E) Wilcoxon test (paired) or (I) Kruskall-Wallis test. ns = not significant; ***P < 0.001; ****P < 0.0001. Scale bar: 5 µm [(B), (C), (H)], 10 µm [(K) top and right, (L), (M)], 20 µm [(A), (G), (K) bottom)].

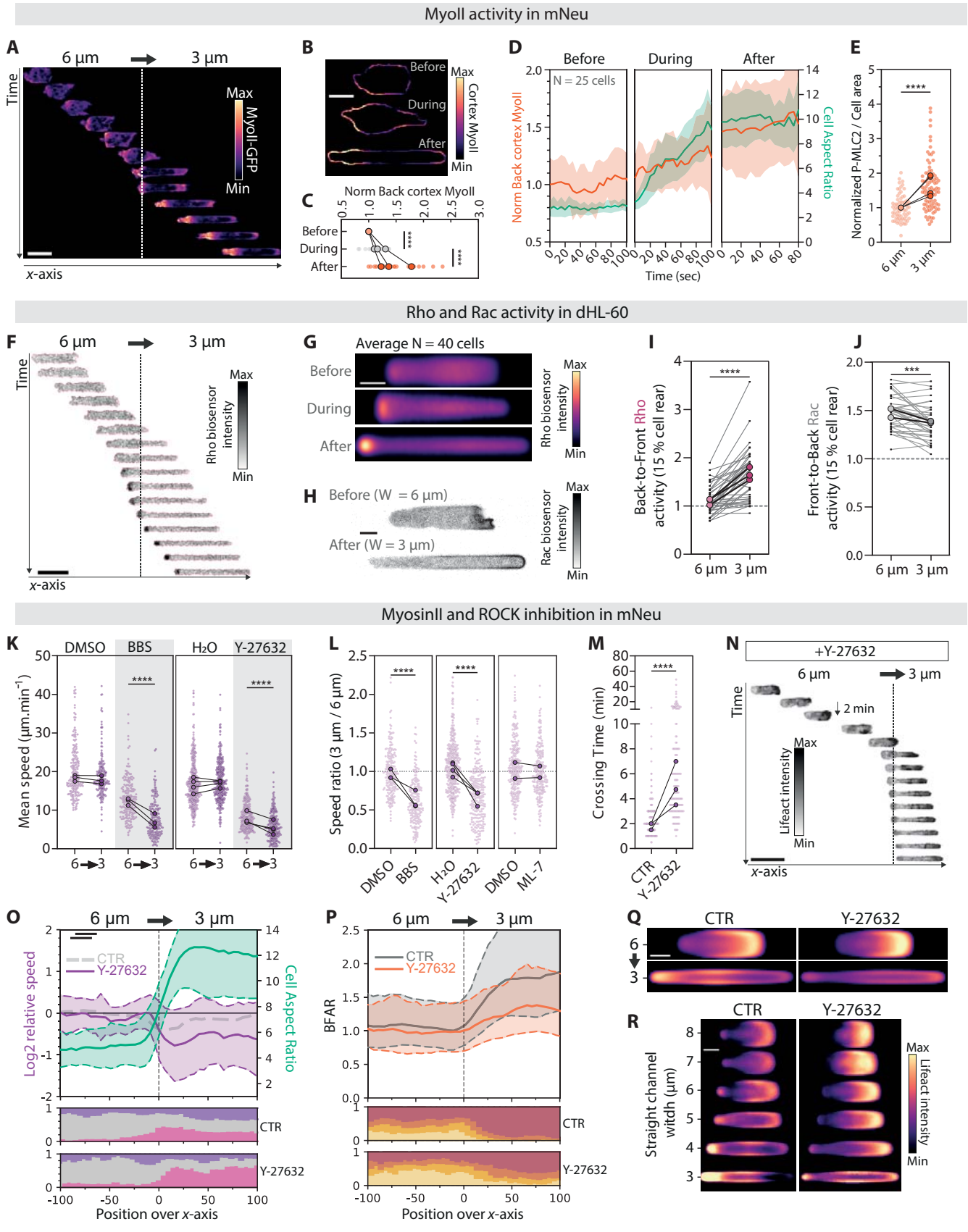

MyoII activity in mNeu
A
6 µm
3 µm
Time
Max
MyoII-GFP
Min
x-axis
B
Before
During
After
Max
Cortex MyoII
Min
C
Norm Back cortex MyoII
Before
During
After
D
Before
During
After
N = 25 cells
Norm Back cortex MyoII
Cell Aspect Ratio
Time (sec)
E
Normalized P-MLC2 / Cell area
****
6 µm
3 µm
Rho and Rac activity in dHL-60
F
6 µm
3 µm
Time
Rho biosensor intensity
Max
Min
x-axis
G
Average N = 40 cells
Before
During
After
Rho biosensor intensity
Max
Min
H
Before (W = 6 µm)
After (W = 3 µm)
Rac biosensor intensity
Max
Min
I
Back-to-Front Rho activity (15 % cell rear)
****
6 µm
3 µm
J
Front-to-Back Rac activity (15 % cell rear)
***
6 µm
3 µm
MyosinII and ROCK inhibition in mNeu
K
DMSO
BBS
H2O
Y-27632
Mean speed (µm.min-1)
****
6→3
L
Speed ratio (3 µm / 6 µm)
****
DMSO
BBS
H2O
Y-27632
DMSO
ML-7
M
Crossing Time (min)
****
CTR
Y-27632
N
+Y-27632
6 µm
3 µm
Time
2 min
Lifeact intensity
Max
Min
x-axis
O
6 µm
3 µm
Log2 relative speed
Cell Aspect Ratio
CTR
Y-27632
CTR
Y-27632
Position over x-axis
P
6 µm
3 µm
BFAR
CTR
Y-27632
CTR
Y-27632
Position over x-axis
Q
CTR
Y-27632
6
3
R
CTR
Y-27632
Straight channel witdh (µm)
Max
Lifeact intensity
Min

Fig. 5. Myosin II is required for neutrophil migration adaptation to confinement strength. (**A** to **D**) Migration of MyoII-GFP expressing neutrophil in size-transition microchannel. (A) Representative kimograph (A) and MyoII-GFP cortical mapping (B). Average back cortical MyoII intensity (C) and its evolution over time (D), n = 25 cells. (E) Normalized P-MLC2 levels; n = 73 cells (6 µm); n = 91 cells (3 µm). (**F** to **J**) Migration of dHL-60 expressing Rho activity reporter (Anillin-RBD) and Rac activity reporter (Pak-PBD) in size-transition microchannel. Representative kimograph (F) and average mapping (G) Rho reporter, n = 40 cells. (H) Representative images of one dHL-60 expressing Rac reporter. Back-to-Front Rho activity of n = 40 cells (I) and front-to-Back Rac activity of n = 35 cells, in 6 µm and 3 µm width sections. (**K** and **L**) Effect of MyoII inhibitor (Blebbistatin, BBS), ROCK inhibitor (Y-27632) and MLCK inhibitor (ML-7) on mNeu migrating in size-transition microchannel. Average speeds (K), speed ratios (L), n > 180 cells for each condition. (**M** to **R**) Effect of ROCK inhibitor (Y-27632) on migration and actin dynamics in size-transition microchannels. Crossing time (M) and representative kymograph (N) of Y-27632 treated Lifeact-EGFP mNeu. Evolution of speed (O) and BFAR (P) over the *x* position; n = 95 cells. Average mapping of Lifeact-EGFP intensity in size-transition (Q) and straight (R) microchannels. Data are pooled from four [(E), (K) Y-27632, (L) Y-27632], three [(C), (D), (G), (I), (K) Blebbistatin, (M), (Q)], or two [(J), (L) ML-7, (R)] independent experiments. Data are one representative [(O) and (P)] of 3 independent experiments. Data were analyzed by [(C), (I), (J), (K), (L)] Wilcoxon test, or [(E), (M)] Mann Whitney test. ns, not significant, ***P < 0.001, ****P < 0.0001. Scale bar: 5 [(B), (G), (H), (Q), (R)], 10 (A), 20 [(F), (N)] µm.

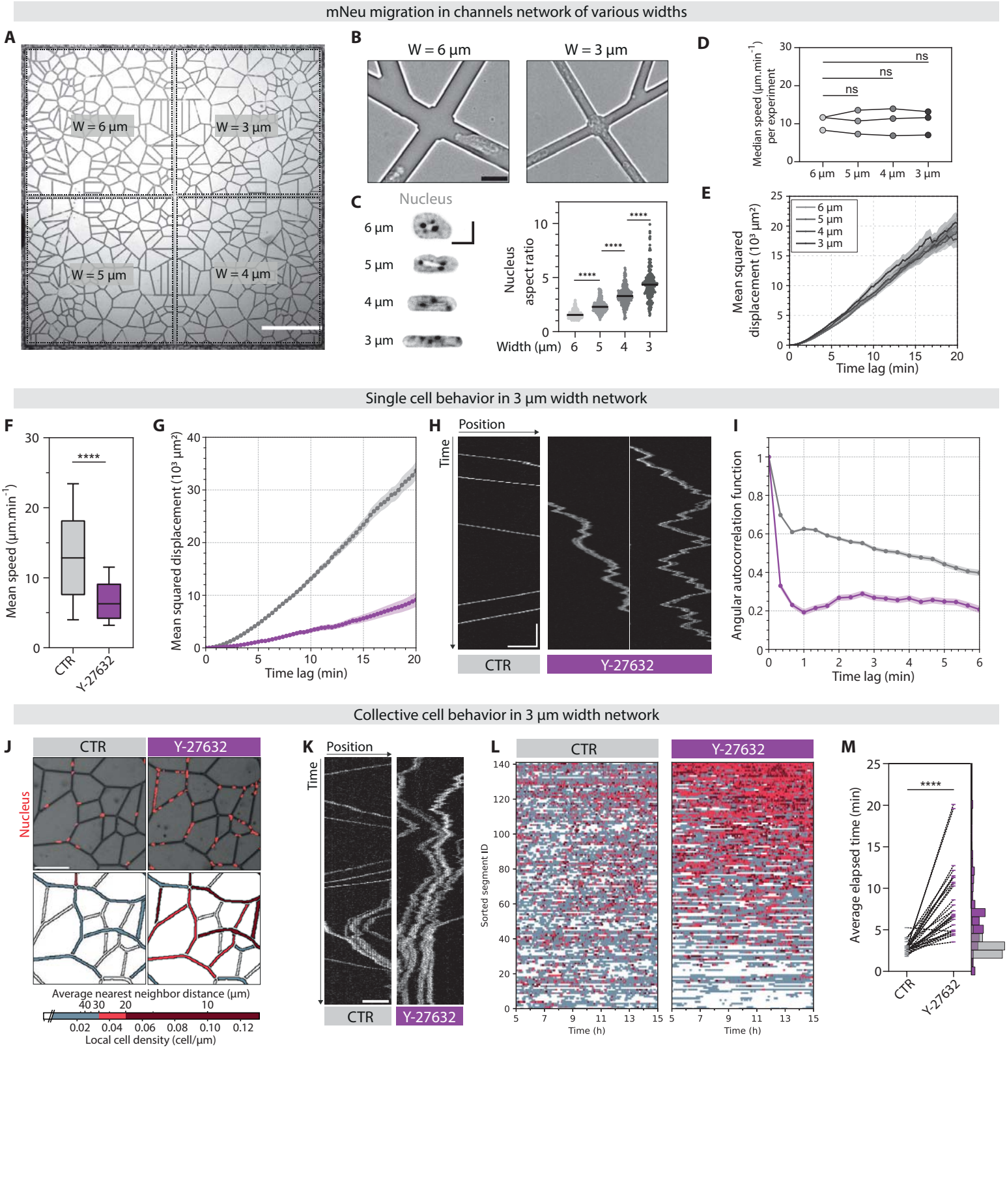

mNeu migration in channels network of various widths
A
W = 6 µm
W = 3 µm
W = 5 µm
W = 4 µm
B
W = 6 µm
W = 3 µm
C
Nucleus
6 µm
5 µm
4 µm
3 µm
Nucleus aspect ratio
Width (µm) 6 5 4 3
****
D
Median speed (µm.min-1) per experiment
ns
6 µm 5 µm 4 µm 3 µm
E
Mean squared displacement (10³ µm²)
6 µm
5 µm
4 µm
3 µm
Time lag (min)
Single cell behavior in 3 µm width network
F
Mean speed (µm.min-1)
****
CTR
Y-27632
G
Mean squared displacement (10³ µm²)
Time lag (min)
H
Position
Time
CTR
Y-27632
I
Angular autocorrelation function
Time lag (min)
Collective cell behavior in 3 µm width network
J
CTR
Y-27632
Nucleus
Average nearest neighbor distance (µm)
40 30 20 10
0.02 0.04 0.06 0.08 0.10 0.12
Local cell density (cell/µm)
K
Position
Time
CTR
Y-27632
L
CTR
Y-27632
Sorted segment ID
Time (h)
M
Average elapsed time (min)
****
CTR
Y-27632

Fig. 6. ROCK is essential for efficient trafficking of large number of neutrophils in a complex capillary-like network. (**A** to **E**) Migration of mNeu in a channels network device. (A) Image of the device (and magnifications in (B)) containing four quadrants of 4 µm height and different widths, connected by a 20 µm-wide central channel. mNeu are loaded into a surrounding reservoir (50 µm height) and spontaneously migrated into the network. (C) Representative images of Hoechst-stained mNeu nuclei (left) and quantification of nuclear AR (Right), n > 275 cells for each width. (D) Median speed per experiment and (E) average mean-square displacement (MSD) versus time-lag, n > 1000 trajectories. (**F** to **I**) Migratory behavior of individual mNeu treated or not with Y-27632, in 3 µm width quadrant (intersections excluded). Distribution of cell mean speed (F) and average MSD versus time-lag, n > 200 trajectories. Representative kimograph (H) and quantification of the angular autocorrelation function versus time-lag (I). (**J** to **M**) Collective behavior of mNeu treated or not with Y-27632, in 3 µm width quadrant (intersections excluded). (J) Spatial distribution of mNeu (top) and estimated cell density per network segment (bottom). Red and brown colors indicate cell density values above 0.03 cell/µm and 0.05 cell/µm, respectively. White indicates segments with no cell trajectory data. (K) Representative kimograph of mNeu in segments with high local cell density. (L) Temporal evolution of mNeu cell density across 140 network segments. Each row represents the same segment under both conditions. (M) Average elapsed time at high cell density values (>0.03 cell/µm). 40 individual segments randomly sampled. Data were analyzed by [(D) and (M)] Wilcoxon test, or [(C) and (F)] Mann Whitney test. ns, not significant, ****P < 0.0001. Scale bar 500 (A), 100 (J), 50 [(H) and (K)], 10 (B), 5 (C) µm.

Supplementary Materials for

Adaptive motility enables neutrophils to rapidly navigate confined capillaries

Mathieu Deygas, Mathilde Bernard, Pierre Nivoit, Henry De Belly, Alexandre Deslys, Theresa Jakuszeit, Damien Cuvelier, Moira Garcia-Gomez, Lucie Barbier, Li Wang, Mathieu Maurin, Emmanuel Tejerina, Oumaima Baaziz, Emmanuel Terriac, Rafaele Attia, Anna Kniazeva, Serge Garbay, Marina Ortega-Zapero, Angela Saez, Raquel Gomez-Bris, Pilar Gonzalo, Jose M. Gonzalez-Granado, Vicente Andrés, Orion D. Weiner, Ana-Maria Lennon-Duménil, Guillaume Duménil, Matthieu Piel; Pablo Vargas

Corresponding authors:
mathieu.deygas@inserm.fr (M.D.)
matthieu.piel@curie.fr (M.P.)
pablo.vargas@inserm.fr (P.V.)

The PDF file includes:

Supplementary Materials and Methods
Figs. S1 to S5
Table S1
Captions for Movies S1 to S21

Other Supplementary Materials for this manuscript include the following:

Movies S1 to S21
Data files S1 to S3
MDAR Reproducibility Checklist

SUPPLEMENTARY MATERIALS AND METHODS

Microfabricated devices

Photolithography

All microdevices used for this work were designed and prepared as follows. First, chrome photomasks were fabricated by JD photo Data (UK) from our designs with specific dimensions (negative pattern). Next, using photolithography technique, Si wafers were photopatterned with an SU-8 negative photoresist. The obtained Si wafers were subsequently silanized and a thick layer of Polydimethylsiloxane (PDMS) (RTV615, Neyco) was poured over the wafer and cured at 65°C for at least 2 hours. PDMS was peeled off the Si wafer and used to prepare a replica mold using epoxy.

Microchannel preparation

Microchannels experiments were performed as previously described (*73*). Briefly, A 10-to-1 mixture of PDMS (Neyco, RTV615) was poured into the custom-made epoxy molds. PDMS crosslinking was obtained after 2 hours at 65°C. PDMS chips were peeled off from the epoxy mold using a blade, cut at the edges, then 2.5 mm holes were drilled in the PDMS chamber in a region near the entry of microchannels, as a reservoir for cell loading. PDMS chamber and 35-mm glass-bottom dish (WPI, FD35-100) were cleaned and plasma activated before being bound to each other. The binding was left to strengthen in a 65°C oven for 15 min.

Microchannel coating

For surface functionalization, the PDMS surfaces were plasma activated during 1 min and incubated with the coating solution at room temperature during 30 min. For most experiments, microchannels were coated with 10 µg/ml fibronectin (Sigma-Aldrich, F1141). When specified, microchannels were coated with 10 µg/ml collagen (Advanced BioMatrix, 5057), 10 µg/ml recombinant Mouse ICAM-1/CD54 (Fisher Scientific, 18378957), 1 mg/ml pLL-PEG or 50 mg/ml Pluronic-F127 (MedChemExpress, HY-D1005). After the incubation step, PDMS chambers were washed three times with 1x PBS then incubated with complete medium (containing drugs when specified) for 2 hours at 37°C and 5% CO_2 before loading of 1×10^5 cells per hole.

Capillary-network-like device

This microfluidic device was fabricated by photolithography as described above. The channel interconnections were inspired by a Voronoi-like organization and the method was used as previously described (*74*). The device consists of four repeated channel networks, identical in layout and height (4 µm) but differing in width (6, 5, 4, and 3 µm). These four networks are

arranged as quadrants and separated by a central channel 20 μm wide. Each quadrant measures 1.2 mm per side. The four quadrants are surrounded by a cell reservoir 100 μm in height and 200 μm in width. Two 1.5-mm-diameter holes were punched on opposite sides of the device before bonding the PDMS to a FluoroDish, as described previously. The assembled device was then placed in a vacuum chamber for 10 min under vacuum, followed by 1 min of plasma treatment. Finally, 5×10^5 cells were directly loaded into one of the inlet holes, and the device was completely filled with culture medium.

Cell isolation and culture

Mouse bone marrow derived dendritic cells (BMDCs)

The BMDCs were obtained by differentiation of bone marrow precursors for 10 days in BMDC media composed of IMDM (iscove's modified dulbecco's medium) Glutamax medium supplemented with fetal bovine serum (10%), penicillin-streptomycin solution (100 U/ml), and 50 μM β-mercaptoethanol (Thermo Fisher Scientific, 31350010) and granulocyte-macrophage colony-stimulating factor (GM-CSF)-containing supernatant (50 ng/ml) obtained from transfected J558 cells, as previously described (*49*). At day 10, semi-adherent cells were collected by carefully flushing with BMDC media after discarding the floating cells. Full differentiation was assessed by flow cytometry analysis of CD11c and CD80 expression.

Mouse T cells

Whole spleens were harvested from mice then dissociated in 1X phosphate-buffered saline (PBS 1X) (Thermo Fisher Scientific, 1234) into single-cell suspensions by passing the splenocytes through a sterile 70 μm mesh nylon strainers (Falcon, 352350). Naïve CD4 T cells from mouse splenocytes were isolated by immunomagnetic negative selection, using the EasySep Mouse naïve CD4 T Cell Isolation Kit (StemCell, 19765). Isolated T cells were activated using monoclonal antibodies against the ε chain of mouse CD3 (subunit of the TCR complex) and the mouse CD28 co-stimulatory molecule for 24 hours and expanded in RPMI 1640 Medium containing 10% fetal bovine serum, 1% non-essential amino acids (Thermo Fisher Scientific, 11140035), 100 U/mL penicillin-streptomycin (Thermo Fisher Scientific, 15140122), 1mM sodium pyruvate (Thermo Fisher Scientific, 11360070), 50 μM β-mercaptoethanol and recombinant 100U/mL interleukine-2 (Preprotech, 212-12). T cells were used after 6 days of culture.

Mouse NK cells

Fresh whole spleens were harvested from mice then dissociated in PBS into single-cell suspensions by passing the splenocytes through a sterile 70 µm mesh nylon strainers (Falcon, 352350). Subsequently, NK cells were enriched by negative selection with magnetic nanobeads using the MojoSort Mouse NK Cell Isolation Kit (Biolegend, 480050) according to the manufacturer's instructions. NK enrichment was assessed by flow cytometry analysis of $NK1.1^{+}/CD3^{-}$ expressing cells. NK cells were cultured in 12-well flat-bottomed plates (Nest, cat. 712001) at a concentration of 1×10^6 cells/ml in culture media containing RPMI 1640 medium supplemented with FBS (10 %), non-essential amino acids (1 %), HEPES buffer, β-mercaptoethanol (55 µM), and recombinant interleukine-15 (7 nM) (BioLegend, 566302). NK cells were used after 4 to 5 days of culture.

Cell lines generation and culture

The human myeloid leukemia-derived pro-myelocytic cell line HL-60, kind gift of Fernando Sepulveda (Institut Imagine, Paris, France), was maintained in RPMI-1640 medium containing 10% heat-inactivated FBS, 20 mM HEPES pH 7.2, and penicillin-streptomycin (100 U/ml). To generate neutrophil-like cells, HL-60 cells were differentiated into dHL-60 in culture medium containing 1.3% DMSO (Sigma Aldrich, D2438) for 5 to 6 days with a change to fresh medium every other day. HL-60 cell lines expressing Rac biosensor (Pak-PBD), Rho biosensor (Anillin-RBD mCherry), as well as HL-60 mSin-KO and Rictor-KO cell lines were generated and maintained in the laboratory of Orion D. Weiner (*44*, *61*, *62*).

To obtain HL-60 overexpressing GFP-lamin-A, WT HL-60 were transduced by viral particles containing lentiviral plasmid for the genome integration of lamin-A fused with N-terminal EGPF. To obtain viral particles, HEK293T cells, kind gift of Ivan Mikaelian (CRCL, Lyon, France), were cultured in DMEM supplemented with 10% FBS, were used to generate lentiviral particles for GFP-lamin A expression in HL-60 cell line. Lentiviral packaging plasmids pMD2.G (0.3 µg) and psPax2 (0.8 µg), along with 0.9 µg of pCSII-GFP-laminA (obtained by cloning GFP-lamin A from Plasmid 206027 on Addgene into pCSII-EF-MCS backbone) were transfected to 1.6×10^6 HEK293T in a well of 6-well plate using Lipofectamine 2000 transfection reagent (ThermoFisher Scientific, 11668027). After 24h, media was changed by HL-60 culture media. The culture supernatant containing lentiviral particles was collected after 48 h. Lentiviral particles supernatants were filtered with 0.45 µm filter, mixed gently with 10 µg/ml protamine sulfate (Sigma Aldrich, 1.10123) and added to 1×10^5 HL-60 cells for spinfection (1000*g* for 2 hours at 35°C). Cells were then sorted by flow cytometry to select GFP^{+} cells.

Microscopy

Microscopy for Rho/Rac biosensor and mTORC2 deficient cell lines imaging

Imaging was performed using a Nikon Ti2-E body scope configured with a CrestOptics X-Light V3 confocal spinning disk system, a Lumencor Celesta light engine, Nikon 10× CFI Plan Apo Lambda objective, an Okobox temperature and CO2 controlled environment, and a Photometrics Kinetix sCMOS camera. The camera was run in a 2 × 2 binning mode with a set exposure time of 200 ms for all channels. All videos are taken with a frame interval of 10 s between exposures. All videos were taken at 37°C with 5% CO_2 for the duration of imaging.

All images were exported from the MetaMorph acquisition software (Molecular Devices) as .tiff files and edited using Fiji (1.54n). Stacks were registered using Stackreg plugin or using SIFT (Scale Invariant Feature Transform) multichannel plugin.

Atomic force microscopy

Suspended dHL60 cells were plated on non-coated glass-bottomed 35-mm dishes (FluoroDish, WPI) and allowed for cell sedimentation for 30 min and kept at 37°C under an inverted light microscope (Axio Observer.Z1; Zeiss) equipped with an atomic force microscopy (AFM) head (NanoDrive; NanoSurf). The wedge cantilever is made from a tipless probe (HQ:NSC35/tipless/Cr-Au; MicroMasch) using UV glue (NOA81; Norland Products Inc) and calibrated by the thermal noise method. The microcantilevers were fixed on a NanoSurf holder and mounted on the AFM head. The cantilever was lowered on the cell to a preset height with a constant speed of 5 μm/s, and the resulting varying force and cantilever height were recorded over time. At the same time, fluorescence images of the confined cell were recorded every 1 s using a 40× NA 1.3 oil objective to control the presence of the cell under the cantilever. All microscopy equipment was placed, and experiments were carried out in an isolation box (Nanosurf). Cell response force were measured on the basis of AFM data. We use the peak force after each approaches a proxy of the nuclear envelope stiffness as we assume the nucleus deformation is achieved at constant volume.

Drugs and dyes

For visualization of the nucleus in live cells, cells were preincubated for 30 min with 10 μg/ml of Hoechst 33342 (ThermoFischer, H1399). For microtubules and centrosome visualization, Spy650-tubulin (Spyrochrome, Cytoskeleton, CY-SC203) was diluted 1:1000 in media that was used

during migration assay. For visualization of intracellular calcium levels, cells were preincubated with 2 µM Fluo8-AM (BioValley, AAT-21082) before washing and imaging.

For experiments with compounds, 1 µM nocodazole (MedChemExpress, HY-13520), 25 µM N-(p-Amylcinnamoyl) anthranilic acid (ACA) (MedChemExpress, HY-118628), 20 µM Y-27632 (MedChemExpress, HY-10071), 25 µM Blebbistatin (MedChemExpress, HY-13813), 25 µM ML-7 (MedChemExpress, HY-15417), 1 mM ethylene glycol tetraacetic acid (EGTA) (MedChemExpress, HY-D0861), 40 µM Gadolinium chloride ($GdCl_3$) (Tocris, 4741), 2.5 µM BAPTA-AM (MedChemExpress, HY-100545), were diluted in media. Media containing indicated compound concentration was used to preincubate cells and channels 30 min prior cell loading, and during the migration assay.

Immunofluorescence

For P-MLC2 immunostaining, neutrophils were prepared as mentioned above, plated in microchannels, and incubated for 2 to 3 hours at 37°C to let them migrate in large and narrow channels. Cells were fixed with 4% paraformaldehyde (Thermo Scientific, 047377.9L) for 20 min at 37°C and washed with PBS. PDMS device was gently removed by first unsticking PDMS from coverslips with razor blades and then pulling vertically with tweezers. For lamin A/C immunostaining, 1×10^5 neutrophils were resuspended in 100 µl of optiMEM (Gibco, 31985-070) media and plated in wells of 96-well glass bottom plates for 30 min at 37°C. OptiMEM was then replaced by complete media for 30 min before fixation with 4% paraformaldehyde for 20 min at 37°C and washed with PBS.

For both staining, cells were permeabilized with 0.1 % Triton X-100 (Sigma-Aldrich, T8787) for 10 min at room temperature, washed and blocked with PBS- 3% BSA (Euromedex, 04-100-812-E) overnight at 4°C. Cells were with stained with rabbit anti-pMLC2 antibody or mouse anti-lamin A/C antibody for 24 hours at 4°C, washed, stained with a goat anti-rabbit Alexa Fluor 647 antibody or a goat anti-Mouse Alexa Fluor 647 antibody (for 1 hour at RT, and washed again. Cells were stained for 5 min with DAPI (Invitrogen, D1306) and the coverslip was mounted on a glass slide with Fluoromount G (Molecular probes). Images were taken with the spinning-disc confocal microscope, with a 40× (for pMLC2) and 60× (lamin A/C) objective. *Z*-stacks of 20 to 40 slices every 0.25 µm were taken. Image analysis was performed using ImageJ/Fiji software. Z max projection of Phalloidin and DAPI signals was used for cell area or nucleus segmentation, and P-MLC2 or lamin A/C mean intensity was measured within cell area and nucleus respectively (10

slices containing highest intensity). Quantifications represented mean intensity of individual cells and z max projection of signal was represented.

Flow cytometry

Up to $5x10^5$ cells were placed per well of a U-bottom 96-well plate for staining then centrifuged at 300 g for 5 min at 4°C to spin down. Cells were resuspended in staining buffer (PBS supplemented with 1% FBS and 2 mM EDTA) for 30 min at 4°C and surface antibodies were used for staining. Files were analyzed using FlowJo (BD Biosciences v10.10.1).

Protein immunoblots

Neutrophils (1×10^6) were lysed in 50 µl of Cell Lysis Buffer II (Invitrogen, FNN0021) containing a protease and phosphatase inhibitor cocktail (Halt, Thermo Fisher Scientific) on ice for 30 min, with vortexing at 10-min intervals. Protein lysate was cleared by centrifugation at 18,000*g* for 10 min at 4°C. Lysates were supplemented with Laemmli SDS sample buffer (reducing, 6X, Thermo Scientific Chemicals, J61337.AD) and then boiled at 95°C for 5 min. 15 µL of lysate per sampled was resolved by SDS-PAGE on a NuPAGE 4-12% Bis-Tris polyacrylamide gel (Invitrogen, NP0335BOX) at 200 V at room temperature. After electrophoresis, the proteins were transferred onto iBlot 2 PVDF (polyvinylidene fluoride membranes) (Invitrogen, IB24002) using the iBlot 2 gel transfer device (P0 program, 7 min). Membranes were blocked with 5% BSA in TBS-T for one hour at room temperature. Membranes were cut according to the molecular weight of the protein of interest. This allowed us to blot different proteins on the same lane. Membranes were incubated with primary antibody in 5% BSA in a wash buffer composed of DPBS (Gibco, 14190144) supplemented with 0.1% Tween-20 (Thermo Scientific, 85113) for one hour at room temperature, then washed 3 × 7 min in wash buffer. Membranes were incubated with secondary antibody in 5% BSA in wash buffer, for one hour at room temperature, then washed 3 × 7 min in wash buffer. Protein bands were revealed by enhanced chemiluminescence using SuperSignal West Pico PLUS Chemiluminescent substrate (Thermo Scientific, 34580) on a ChemiDoc (BioRad).

Figure S1

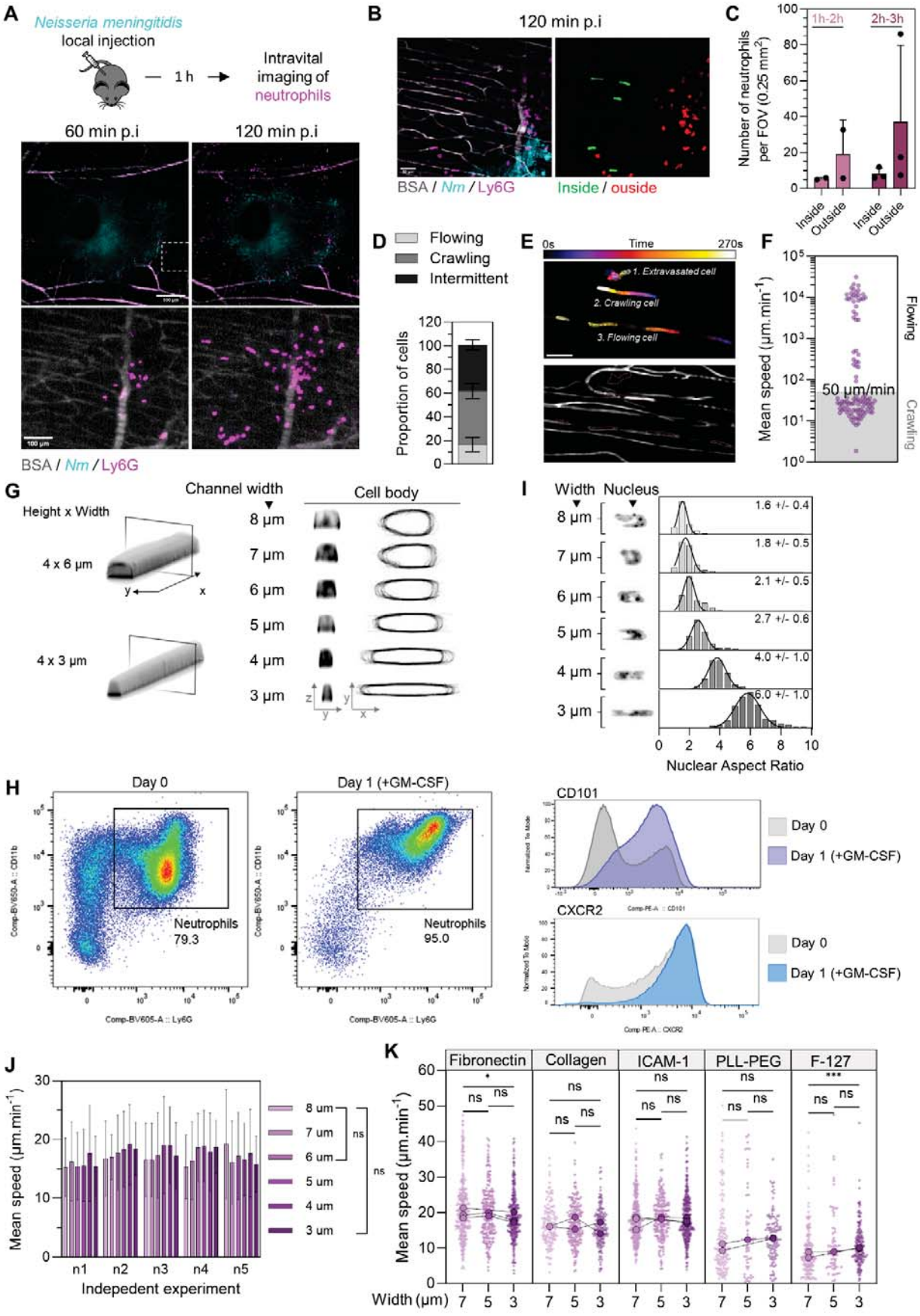

A
Neisseria meningitidis
local injection
1 h
Intravital imaging of neutrophils
60 min p.i
120 min p.i
BSA / Nm / Ly6G
B
120 min p.i
BSA / Nm / Ly6G
Inside / ouside
C
1h-2h
2h-3h
Number of neutrophils per FOV (0.25 mm²)
Inside
Outside
Inside
Outside
D
Flowing
Crawling
Intermittent
Proportion of cells
E
0s
Time
270s
1. Extravasated cell
2. Crawling cell
3. Flowing cell
F
Mean speed (µm.min⁻¹)
50 µm/min
Flowing
Crawling
G
Channel width
Cell body
Height x Width
4 x 6 µm
4 x 3 µm
8 µm
7 µm
6 µm
5 µm
4 µm
3 µm
I
Width
Nucleus
1.6 +/- 0.4
1.8 +/- 0.5
2.1 +/- 0.5
2.7 +/- 0.6
4.0 +/- 1.0
6.0 +/- 1.0
Nuclear Aspect Ratio
H
Day 0
Day 1 (+GM-CSF)
Neutrophils
79.3
Neutrophils
95.0
Comp-BV605-A :: Ly6G
Comp-BV650-A :: CD11b
CD101
CXCR2
Day 0
Day 1 (+GM-CSF)
J
Mean speed (µm.min⁻¹)
8 um
7 um
6 um
5 um
4 um
3 um
ns
n1
n2
n3
n4
n5
Indepedent experiment
K
Fibronectin
Collagen
ICAM-1
PLL-PEG
F-127
Mean speed (µm.min⁻¹)
Width (µm)
ns
*
***

Fig. S1.

(**A**) Experimental strategy to observe endogenous neutrophil trafficking in subcutaneous blood capillaries by spinning-disk-confocal intravital imaging. Bottom, 5X objective spinning disc-confocal images of subcutaneous blood capillaries (gray, fluorescent BSA), endogenous neutrophils (magenta, Ly6G), and *Neisseria meningitidis* (cyan) at 60 min and 120 min post-infection. Scale bar: 500 µm. Magnification of white square indicated in top image. Scale bar: 100 µm. (**B**) Left, 25X objective spinning disk-confocal images of subcutaneous blood capillaries (gray, fluorescent BSA), endogenous neutrophils (magenta, Ly6G), and *Neisseria meningitidis* (cyan) at 120 min post infection. Scale bar: 50 µm. Right, neutrophils located inside (green) or outside (red) capillaries. (**C**) Number of neutrophils inside and outside capillaries per field of view (0.25 mm^2) between 1h and 2h and between 2h-3h post-infection. Bars represent mean +/- SD from two (1h-2h) or three (2-3h) independent experiment. (**D**) Percentage of flowing, crawling and intermittently flowing and crawling cells inside subcutaneous capillaries from 3 independent experiments, n =238 cells. (**E**) Time projection of one field of view, showing a neutrophil migrating outside capillaries (1), a neutrophil crawling inside capillary (2), and a neutrophil intermittently crawling and flowing inside capillary (3). Scale bar: 50 µm (**F**) Mean trafficking speed of individual cells in subcutaneous capillaries. Data are pooled from 3 independent experiments, n = 99 cells. (**G**) Left, 3D reconstruction of a 4 x 6 µm channel section (top) and a 4 x 3 µm channel section using fluorescent dextran. Right, cross sections of Lifeact-EGFP expressing neutrophils and representation of 30 cell contours per channel width. (**H**) FACS quantification of bone marrow neutrophils. Left, Ly6G fluorescence is analyzed in $CD11b^+$ cells at day 0 after isolation and at day 1 (in the presence of GM-CSF). Right, flow cytometry analysis of CD101 and CXCR2 surface expression at day 0 and day 1 in $CD11^+$ $Ly6G^+$ cells. (**I**) Distribution of mean nuclear aspect ratio, from 2 independent experiments. Median +/- SD is indicated for each channel width. 8 µm, n = 80; 7 µm, n = 86; 6 µm, n = 88; 5 µm, n = 118; 4 µm, n = 132; 3 µm, n = 137. (**J**) Mean cell speed +/- SD of five independent experiments in 8 to 3 µm channel widths, presented in Fig.1K. Wilcoxon matched-pairs signed rank test, ns not significant. (**K**) Mean cell speeds of neutrophils migrating in microchannels of 7, 5, 3 µm widths coated with different surface molecules, from 2 or 3 independent experiments. Median of each experiment are represented by paired bigger dots. Fibronectin 10 µg/ml, 7 µm, n = 277; 5 µm, n = 209; 3 µm, n = 289. Collagen 10 µg/ml, 7 µm, n = 134; 5 µm, n = 180; 3 µm, n = 163. ICAM-1 10 µg/ml, 7 µm, n = 303; 5 µm, n = 187; 3 µm, n = 349. PLL-g-PEG 1 mg/ml, 7 µm, n = 145; 5 µm, n = 55; 3 µm, n = 117. Pluronic F-127 5% (w/v), 7 µm, n = 167; 5 µm, n = 62; 3 µm, n = 181. Kruskal-Wallis test, ns not significant, *$P < 0.05$, ***$P < 0.001$.

Figure S2

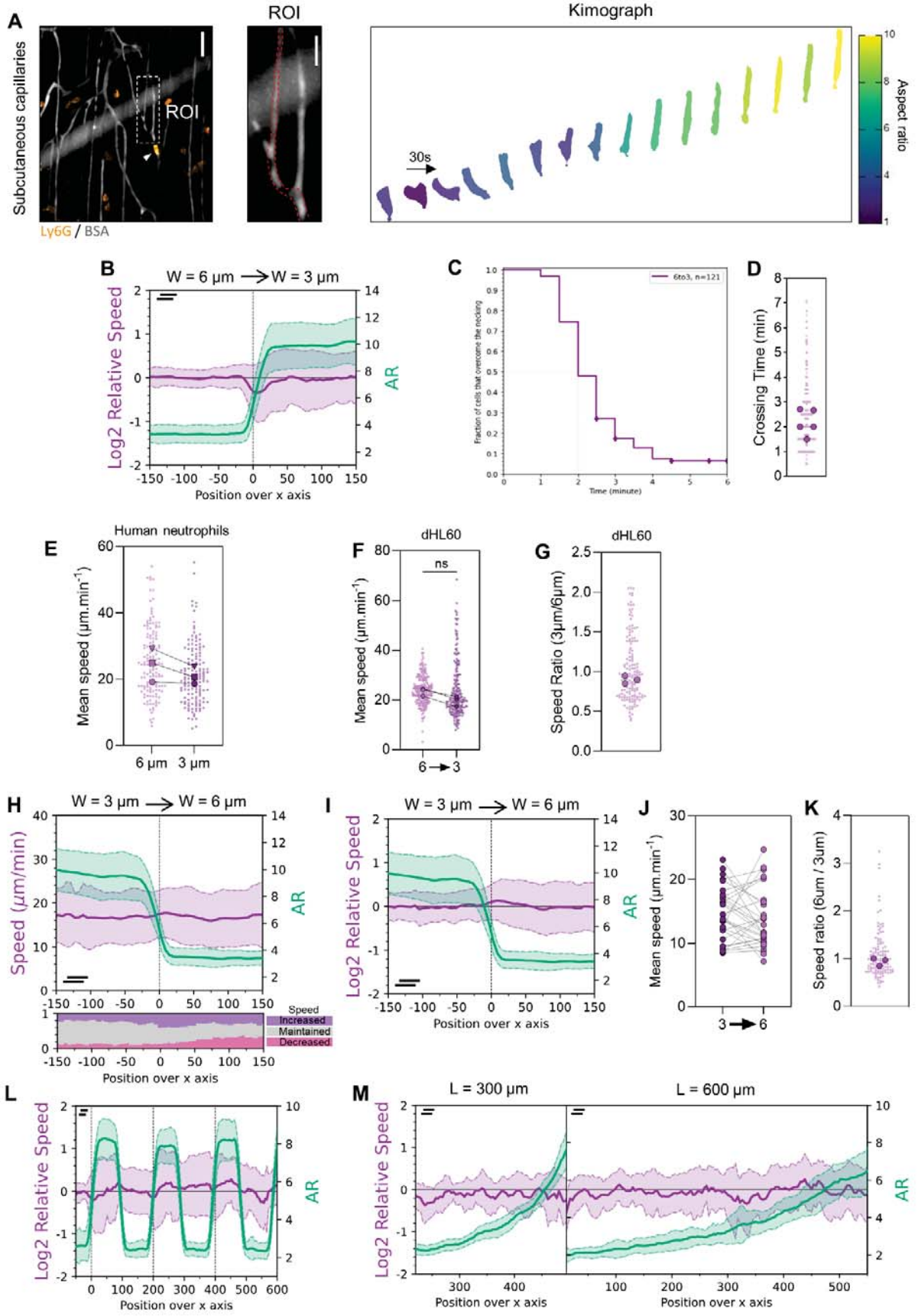

A
Subcutaneous capillaries
ROI
Ly6G / BSA
ROI
Kimograph
30s
Aspect ratio
B
W = 6 µm → W = 3 µm
Log2 Relative Speed
AR
Position over x axis
C
6to3, n=121
Fraction of cells that overcome the necking
Time (minute)
D
Crossing Time (min)
E
Human neutrophils
Mean speed (µm.min-1)
6 µm 3 µm
F
dHL60
ns
Mean speed (µm.min-1)
6 → 3
G
dHL60
Speed Ratio (3µm/6µm)
H
W = 3 µm → W = 6 µm
Speed (µm/min)
AR
Speed
Increased
Maintained
Decreased
Position over x axis
I
W = 3 µm → W = 6 µm
Log2 Relative Speed
AR
Position over x axis
J
Mean speed (µm.min-1)
3 → 6
K
Speed ratio (6um / 3um)
L
Log2 Relative Speed
AR
Position over x axis
M
L = 300 µm
L = 600 µm
Log2 Relative Speed
AR
Position over x axis
Position over x axis

Fig. S2.

(**A**) Example of a mNeu migrating in a subcutaneous capillary exhibiting gradual narrowing. Right, kymograph showing mNeu displacement with color-coded cell aspect ratio. (**B**) Relative speed (Log2) and cell aspect ratio over the *x*-position in a size-transition microchannel (corresponding to figure 2B). Data are one representative of 5 experiments, n = 122 cells. (**C**) Fraction of mNeu crossing the constriction (necking) from 6 to 3 µm-wide channel according to the time. At 2 min, 50 % of mNeu have entirely entered in the 3 µm-wide section. Data are one representative of 5 experiments, n = 121 cells. (**D**) Crossing time or time spent in the necking. Each small dot represents a cell, and bigger dots represent a median of one experiment. From five independent experiment, n = 544 cells. (**E**) Average speeds of primary human blood neutrophils migrating from 6 µm to 3 µm wide section. From 3 independent experiments, n = 144 cells. (**F** and **G**) Average speeds (F) and speed ratio (G) of dHL-60 derived neutrophils migrating from 6 µm to 3 µm wide section. From 3 independent experiments, n = 200 cells. (**H** to **K**) Migration of mNeu in a size-transition channel from 3-to-6 µm width. Evolution of cell AR, speed (H) and Log2 relative speed (I) and cell AR over the *x*-position. Position 0 corresponds to the enlargement from 3 to 6 µm width. Bottom, evolution of the fraction of cells displaying a speed increase, maintenance or decrease over the x axis, compared with the respective mean speed in the 3 µm-wide section. Data are one representative of 3 experiments, n = 86 cells. (J) Average speeds of 30 cells (random) migrating from 3 µm to 6 µm-wide section. (K) Speed ratio: average speed in the 6 µm-wide section normalized by the average speed in the 3 µm-wide section. Each small dot represents a cell, and bigger dots represent a median of one experiment. From 3 independent experiments, n = 119 cells. (**L**) Relative speed (Log2) and cell aspect ratio over the x position in a successive size-transition microchannel (corresponding to Fig. 2G). (**M**) Relative speed (Log2, corresponding to Fig.2J) and cell aspect ratio over the x axis of the funnel-shaped channel of 300 µm length (left) and 600 µm length (right).

Figure S3

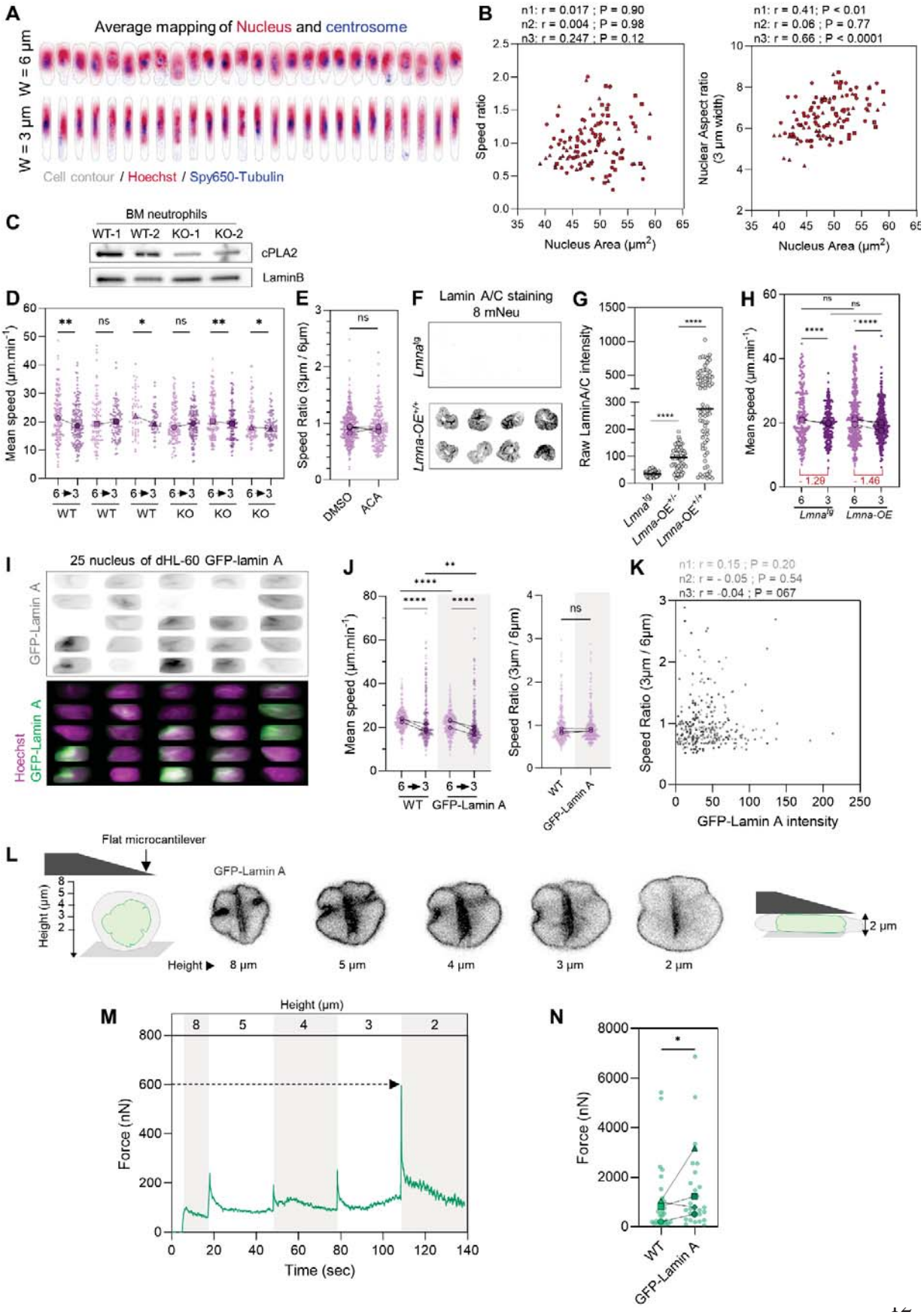

A
Average mapping of Nucleus and centrosome
W = 6 µm
W = 3 µm
Cell contour / Hoechst / Spy650-Tubulin
B
n1: r = 0.017 ; P = 0.90
n2: r = 0.004 ; P = 0.98
n3: r = 0.247 ; P = 0.12
Speed ratio
Nucleus Area (µm²)
n1: r = 0.41; P < 0.01
n2: r = 0.06 ; P = 0.77
n3: r = 0.66 ; P < 0.0001
Nuclear Aspect ratio (3 µm width)
Nucleus Area (µm²)
C
BM neutrophils
WT-1 WT-2 KO-1 KO-2
cPLA2
LaminB
D
Mean speed (µm.min⁻¹)
6►3
WT WT WT KO KO KO
E
Speed Ratio (3µm / 6µm)
DMSO ACA
F
Lamin A/C staining
8 mNeu
Lmna^tg
Lmna-OE+/+
G
Raw LaminA/C intensity
Lmna^tg Lmna-OE+/- Lmna-OE+/+
H
Mean speed (µm.min⁻¹)
- 1.29
- 1.46
Lmna^tg Lmna-OE
I
25 nucleus of dHL-60 GFP-lamin A
GFP-Lamin A
Hoechst
GFP-Lamin A
J
Mean speed (µm.min⁻¹)
6►3 6►3
WT GFP-Lamin A
Speed Ratio (3µm / 6µm)
WT
GFP-Lamin A
K
n1: r = 0.15 ; P = 0.20
n2: r = - 0.05 ; P = 0.54
n3: r = -0.04 ; P = 067
Speed Ratio (3µm / 6µm)
GFP-Lamin A intensity
L
Flat microcantilever
GFP-Lamin A
Height (µm)
Height ▶ 8 µm 5 µm 4 µm 3 µm 2 µm
2 µm
M
Height (µm)
8 5 4 3 2
Force (nN)
Time (sec)
N
Force (nN)
WT
GFP-Lamin A

Fig. S3.

(**A**) Average mapping of cell contour (gray), nucleus (red) and centrosome (blue) for 26 cells migrating from 6 µm to 3 µm width sections. (**B**) Left, absence of correlation between speed ratio and nucleus area. Right, positive correlation between nucleus area and nucleus aspect ratio. From 3 independent experiments, n = 121 cells. Spearman correlation coefficient are indicated for independent experiments (**C**) Western blot showing 70 % reduction of $cPLA_2$ protein level in KO cells. (**D**) Mean speed of WT and $cPLA_2$ mNeu migrating from 6 µm to 3 µm width sections. From 3 independent mice and experiments. (**E**) Speed ratio of DMSO and N-(p-amylcinnamoyl) Anthranilic Acid (ACA, broad $cPLA_2$ inhibitor) treated neutrophils migrating from 6 µm to 3 µm width sections. From 4 independent experiments, n = 342 (DMSO) cells, n = 214 (ACA) cells. (**F**) Lamin A/C immunostaining of mNeu from *Lmna*^{tg} mice (control) and LysM-Cre; Tg-*Lmna* mice (*Lmna-OE*, Lamin A overexpression). (**G**) Quantification of lamin A/C levels by immunostaining in mNeu controls (*Lmna*^{tg}) and mNeu overexpressing lamin A (*Lmna*-OE$^{+/-}$ and *Lmna*-OE$^{+/+}$). *Lmna*^{tg}, n = 69. *Lmna*-OE$^{+/-}$, n = 56; *Lmna*-OE$^{+/+}$, n = 75 cells. Mann Whitney test, two-tailed, **** $P < 0.0001$. (**H**) Mean speed of mNeu control and mNeu overexpressing Lamin A (*Lmna-OE*$^{+/+}$) in 6 and 3 µm width sections, n = 204 (*Lmna*^{tg}) and n = 342 (*Lmna-OE*) cells. Mean speed (µm/min) differences are indicated in red. Data are pooled from 2 (*Lmna*^{tg}) and 3 (*Lmna-OE*) independent experiments. Mann Whitney and Wilcoxon tests. ns, not significant, ****$P < 0.0001$. (**I**) Average mapping of GFP-lamin A intensity for 25 dHL-60 cells overexpressing GFP-lamin A. (**J**) Mean speeds (left) and speed ratios (right) of WT and GFP-lamin A overexpressing dHL-60 cells migrating from 6 µm to 3 µm width sections. From 3 independent experiments, WT, n = 299; GFP-lamin A, n = 290 cells. Mann Whitney test, two-tailed, ** $P < 0.01$, **** $P < 0.0001$. (**K**) Absence of correlation between GFP-lamin A intensity and speed ratio. From 3 independent experiments, n = 290 cells. Spearman correlation coefficient indicated for independent experiments. (**L**) Schematic representation of AFM experimental settings. (**M**) Representative force curve in response to stepwise (30 sec interval) confinement of a dHL-60 cell by the flat microcantilever. (**N**) Measurement of the force increase at 2 µm confinement. From 3 independent experiments, WT, n = 23 cells; lamin A-GFP, n = 24 cells. Mann Whitney test, one-tailed, * $P < 0.05$.

Figure S4

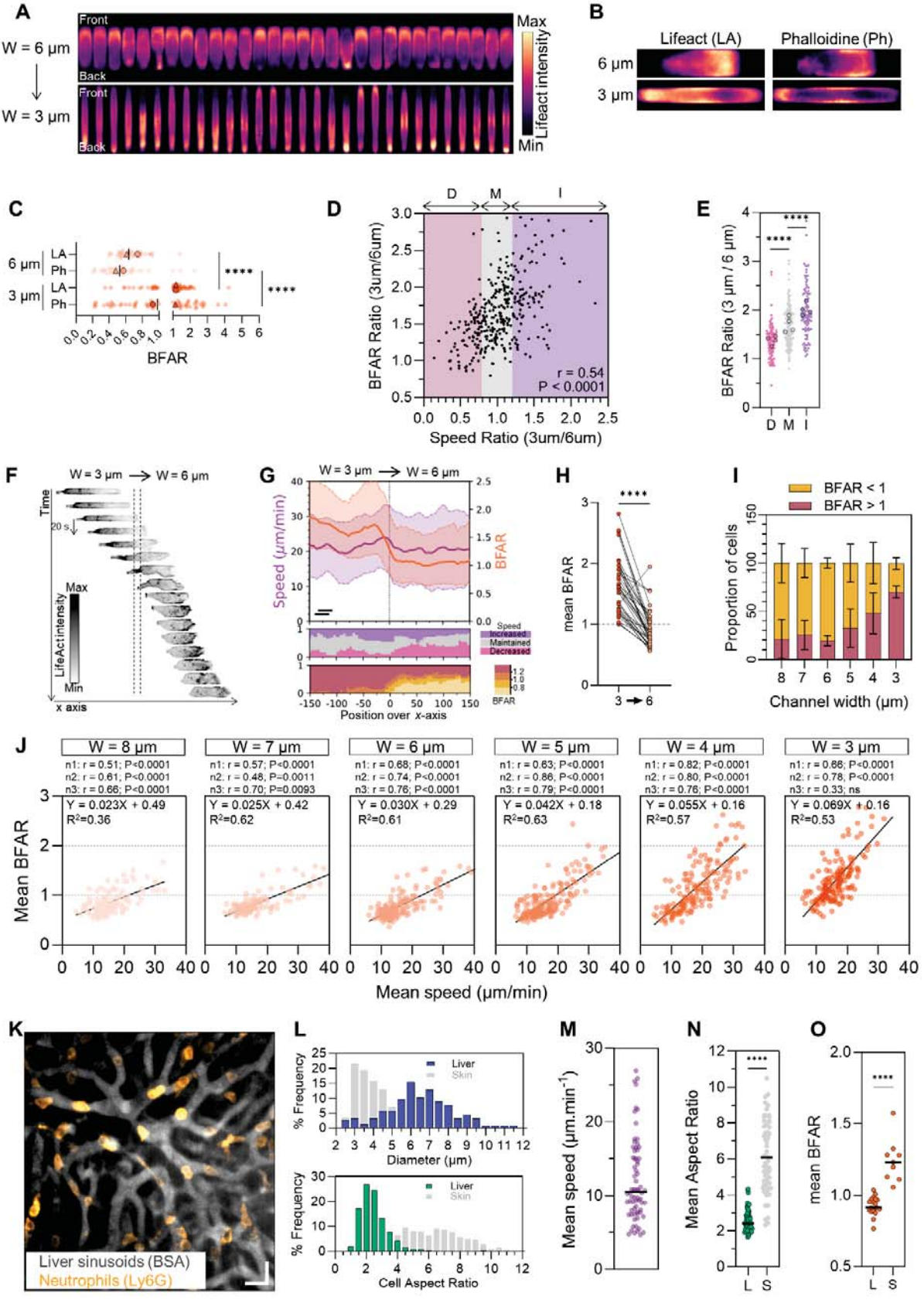

A
W = 6 µm
W = 3 µm
Front
Back
Front
Back
Max
Min
Lifeact intensity
B
Lifeact (LA)
Phalloidine (Ph)
6 µm
3 µm
C
6 µm
LA
Ph
3 µm
LA
Ph
****
****
BFAR
D
D
M
I
BFAR Ratio (3um/6um)
Speed Ratio (3um/6um)
r = 0.54
P < 0.0001
E
BFAR Ratio (3 µm / 6 µm)
****
****
D M I
F
W = 3 µm → W = 6 µm
Time
20 s
Max
LifeAct intensity
Min
x axis
G
W = 3 µm → W = 6 µm
Speed (µm/min)
BFAR
Speed
Increased
Maintained
Decreased
BFAR
Position over x-axis
H
****
mean BFAR
3 → 6
I
BFAR < 1
BFAR > 1
Proportion of cells
Channel width (µm)
J
W = 8 µm
n1: r = 0.51; P<0.0001
n2: r = 0.61; P<0.0001
n3: r = 0.66; P<0.0001
Y = 0.023X + 0.49
R²=0.36
W = 7 µm
n1: r = 0.57; P<0.0001
n2: r = 0.48; P=0.0011
n3: r = 0.70; P=0.0093
Y = 0.025X + 0.42
R²=0.62
W = 6 µm
n1: r = 0.68; P<0.0001
n2: r = 0.74; P<0.0001
n3: r = 0.76; P<0.0001
Y = 0.030X + 0.29
R²=0.61
W = 5 µm
n1: r = 0.63; P<0.0001
n2: r = 0.86; P<0.0001
n3: r = 0.79; P<0.0001
Y = 0.042X + 0.18
R²=0.63
W = 4 µm
n1: r = 0.82; P<0.0001
n2: r = 0.80; P<0.0001
n3: r = 0.76; P<0.0001
Y = 0.055X + 0.16
R²=0.57
W = 3 µm
n1: r = 0.66; P<0.0001
n2: r = 0.78; P<0.0001
n3: r = 0.33; ns
Y = 0.069X + 0.16
R²=0.53
Mean BFAR
Mean speed (µm/min)
K
Liver sinusoids (BSA)
Neutrophils (Ly6G)
L
Liver
Skin
% Frequency
Diameter (µm)
Liver
Skin
% Frequency
Cell Aspect Ratio
M
Mean speed (µm.min⁻¹)
N
****
Mean Aspect Ratio
L S
O
****
mean BFAR
L S

Fig. S4.

(**A**) Average mapping of Lifeact-EGFP of 30 mNeu migrating from 6 µm to 3 µm width sections. Each row represents a cell, in the 6 µm (top) and the 3 µm (bottom) channel. (**B** and **C**) Phalloidin staining of fixed Lifeact-EGFP expressing mNeu in in 6 µm and 3 µm wide channels. (B) Average mapping. 6 µm, n = 35 cells; 3 µm, n = 49 cells. (C) BFAR values. 6 µm, n = 44 cells; 3 µm, n = 61 cells. (**D**) Scatter plot showing the correlation between BFAR ratio and speed ratio. Ratios are defined by the mean values in 3 µm section divided by mean values of 6 µm section for individual cells. Speed decrease (D), maintenance (M) and increase (I) are indicated with colored rectangles. n = 346 cells. Spearman correlation coefficient r = 0.54, P<0.0001. (**E**) BFAR ratios of cells depending on their migratory response to sharp change in confinement strength. n = 90 (D); n = 157 (M); n = 99 (I). (**F** to **H**) Migration of Lifeact-EGFP mNeu in a size-transition channel from 3 µm to 6 µm width. (F) Kimograph of one cell. (G) Evolution of speed and BFAR over the *x*-axis. Data are one representative of 3 experiments, n = 25 cells. (H) Mean BFAR. n = 40 cells. (**I** and **J**) Migration of Lifeact-EGFP mNeu in straight channels of 8 µm to 3 µm width. (I) Proportion of mNeu with a mean BFAR value below or above one. 8 µm, n = 216; 7 µm, n = 210; 6 µm, n = 257; 5 µm, n = 289; 4 µm, n = 271; 3 µm, n = 253 cells. (J) Relation between BFAR and cell speed. Simple linear regression is applied with indicated slope and R squared. 8 µm, n = 132; 7 µm, n = 120; 6 µm, n = 170; 5 µm, n = 187; 4 µm, n = 169; 3 µm, n = 163 cells. Spearman correlation coefficient and P values are indicated for each independent experiments. (**K**) Spinning disk-confocal images of liver sinusoids (gray, fluorescent BSA) and endogenous neutrophils (orange, Ly6G) 2 hours after LPS endotoxemia. Scale bar: 20 µm. (**L**) Top, frequency distribution (percentage) of liver sinusoid diameters. Data are pooled from 4 independent experiments, for a total of 156 segments. Bottom, frequency distribution of cell aspect ratio of neutrophils trafficking inside sinusoids. n=1119 shapes. (**M**) Mean speed of individual crawling cells in liver sinusoids, n = 72 cells. (**N**) Mean cell AR of neutrophils in liver sinusoids (L) and skin capillaries (S). Data of skin condition are the same than in Fig.1. L, n = 69 cells; S, n = 61 cells. (**O**) Mean BFAR of mNeu expressing lifeact-EGFP mNeu migrating in liver sinusoids (L) or skin capillaries (S). L, n = 19 cells; S, n = 9 cells. Each dot represents one cell [(C), (D), (E), (H), (J), (M), (N), (O)] and large dots represent the mean of each experiment [(C), (E)]. Data are pooled from four [(D), (E), (I), (L)], three [(H), (J), (M), (N)] or two [(C), (O)] independent experiments. Data are one representative of three (G) or two (B) independent experiments. Data were analyzed by (H) Wilcoxon test (paired) or [(C), (E), (N), (O)]. ****P < 0.0001.

Figure S5

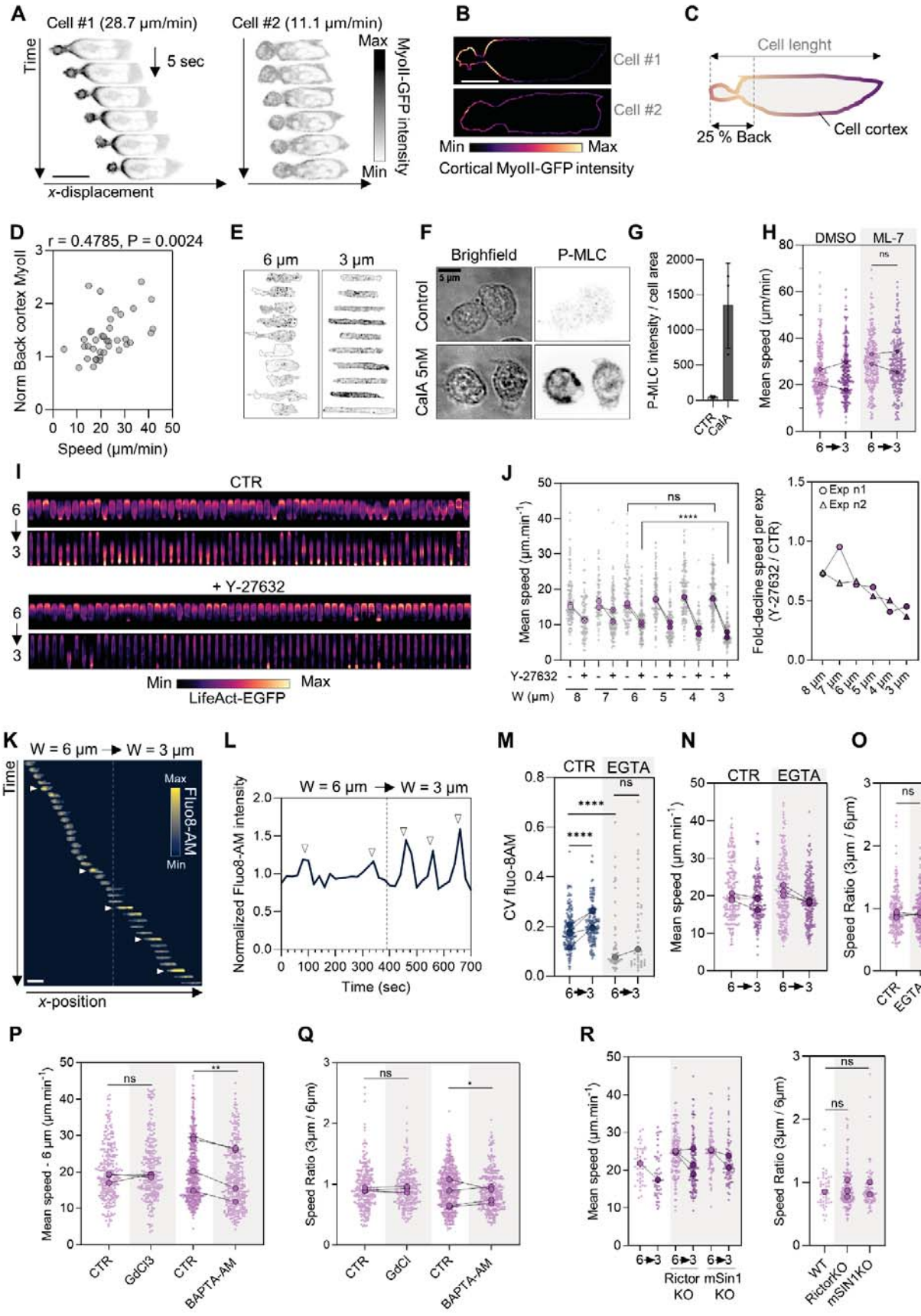

A
Cell #1 (28.7 µm/min)
Cell #2 (11.1 µm/min)
Time
5 sec
x-displacement
Max
Min
MyoII-GFP intensity
B
Cell #1
Cell #2
Min
Max
Cortical MyoII-GFP intensity
C
Cell lenght
25 % Back
Cell cortex
D
r = 0.4785, P = 0.0024
Norm Back cortex MyoII
Speed (µm/min)
E
6 µm
3 µm
F
Brighfield
P-MLC
Control
CalA 5nM
5 µm
G
P-MLC intensity / cell area
CTR
CalA
H
DMSO
ML-7
ns
Mean speed (µm/min)
6→3
I
CTR
+ Y-27632
6
3
Min
Max
LifeAct-EGFP
J
Mean speed (µm.min-1)
ns
****
Y-27632
W (µm)
Fold-decline speed per exp (Y-27632 / CTR)
Exp n1
Exp n2
K
W = 6 µm → W = 3 µm
Time
Max
Min
Fluo8-AM
x-position
L
W = 6 µm → W = 3 µm
Normalized Fluo8-AM intensity
Time (sec)
M
CTR
EGTA
CV fluo-8AM
N
Mean speed (µm.min-1)
O
Speed Ratio (3µm / 6µm)
P
Mean speed - 6 µm (µm.min-1)
CTR
GdCl3
BAPTA-AM
Q
Speed Ratio (3µm / 6µm)
R
Mean speed (µm.min-1)
Rictor KO
mSin1 KO
Speed Ratio (3µm / 6µm)
WT
RictorKO
mSIN1KO

Fig. S5.

(**A** to **D**) Migration of MyoII-GFP expressing mNeu in 6 µm width channel. Representative kimographs (A) of a fast (Cell #1, left) and slow (Cell #2, right) cell and their cortical MyoII-GFP signal (B). (C) Illustration of back cortical MyoII-GFP quantification. (D) Correlation between mean cell speed and back cortical MyoII signal (normalized to total MyoII signal), n = 38 cells. Spearman correlation coefficient = 0.48, P = 0.002 (two tailed). (**E** to **G**) Immunostaining of Phospho-Myosin Light Chain 2 (P-MLC2) of fixed mNeu. (E) Ten representative cells in 6 µm and 3 µm-wide channels. P-MLC2 staining (F) and quantification (G) in control and Calyculin A treated mNeu. (**H**) Average speeds of cells migrating from 6 µm to 3 µm-wide section, treated or not with ML-7. DMSO, n = 257; ML-7, n = 217. (**I**) Average Lifeact-EGFP intensity mapping of control and Y-27632 treated cells in size-transition channels. n = 60 cells. (**J**) Left, average speeds of mNeu in straight channels of different widths (W), treated (+Y) or not (-Y) with Y-27632. n > 80 cells per condition. Right, Relative mean speed (Y-27632 / CTR) related to the left panel. (**K** to **M**) Cytosolic calcium dynamics (Fluo8-AM) in mNeu migrating in a size-transition channel. (K) Representative kymograph (K) and quantification (L) of one cell showing the evolution of Fluo8-AM intensity over the *x*-position. Arrows indicate calcium pulses and vertical dotted line indicates the narrowing. (M) Coefficient variation (Standard deviation / Mean) of Fluo8-AM intensity of control and EGTA (1 mM) treated cells. CTR, n = 165 cells; EGTA, n = 48 cells. (**N** and **O**) Average speeds (N) and speed ratios (O) of mNeu migrating from 6 µm to 3 µm-wide section, treated or not with EGTA (1 mM)., control, n =183, EGTA, n = 204 cells. (**P** and **Q**) Average speeds in the 6 µm width section (P) and speed ratios (Q) of mNeu treated or not with $GdCl_3$ or BAPTA-AM.; CTR (GdCl3), n = 268, GdCl3, n = 228; CTR (BAPTA-AM), n = 472, BAPTA-AM, n = 299 cells. (**R**) Average speeds (left) and speed ratios (right) of dHL-60 cells lacking different core components of the mTORC2 complex (Rictor or mSIN1 CRISPR KO cell lines). WT, n = 48; Rictor KO, n = 123; mSIN1 KO, n = 76 cells. Data are pooled from four [(M) CTR, (P) and (Q) BAPTA-AM], three [(I), (N), (O), (P) and (Q) $GdCl_3$, (R) Rictor KO] or two [(H), (J), (R) mSin1 KO]. Data were analyzed by Mann Whitney test. ns, not significant; *P < 0.05; **P < 0.01; ****P < 0.0001. Scale bar: 10 µm (A), 5 µm (B), 20 µm (K).

Table S1.

	Target	Clone	Supplier	Catalogue nr.	Final concentration used
Intravital imaging					
	CD31	390	Biolegend	102414	10µg/mouse
	CD31	390	Biolegend	102432	10µg/mouse
	CD31	390	Biolegend	102416	10µg/mouse
	Ly6G	1A8	Biolegend	127626	2.5µg/mouse
	Ly6G	1A8	Biolegend	127636	2.5µg/mouse
	Ly6G	1A8	Biolegend	127610	2.5µg/mouse
T cell culture					
	CD28	37.51	BD Biosciences	553295	1µg/mL, soluble
	CD3ε	500A2	BD Biosciences	553238	2µg/mL, coating
Immunoblotting					
Primary antibodies	$cPLA_2$	N/A	Cell Signaling Technology	2832	1:1,000
	Lamin B1	EPR8985 (B)	Abcam	ab133741	1:1,000
Secondary antibodies	Goat Anti-rabbit IgG, HRP-linked Antibody	N/A	Cell Signaling Technology	7074	1:10,000
	Goat anti-Mouse IgG (H+L) Secondary Antibody, HRP	N/A	Thermo Fisher Scientific	31430	1:10,000
Immunofluorescence					
Primary antibodies	Lamin A/C	4C11	Cell signaling Technology	4777	1:500
	pMLC2	N/A	Cell Signaling Technology	3674	1:500
Secondary antibodies	goat anti-rabbit Alexa Fluor 647 antibody	N/A	Invitrogen	A32733	1:1,000
	goat anti-Mouse Alexa Fluor 647 antibody	N/A	Thermo Fisher Scientific	A-21241	1:1,000
Flow cytometry					
	CD11b	M1/70	Sony Biotechnology	1106030	1:500
	CD182 (CXCR2)	SA045E1	Sony Biotechnology	1348045	1:500
	CD101	Moushi101	eBioscience	12-1011-82	1:500
	Ly6G	1A8	Sony Biotechnology	1238195	1:500

Movie S1.
Intravital imaging of skin capillaries and endogenous neutrophils at steady state.

Movie S2.
Intravital imaging of endogenous neutrophils recruitment in skin tissue after *Nm* local injection.

Movie S3.
Intravital imaging of endogenous neutrophils trafficking and migrating in skin capillaries two hours after *Nm* local injection.

Movie S4.
Examples of endogenous neutrophil migratory behavior in skin capillaries.

Movie S5.
Migration of mNeu in straight microchannels of different widths.

Movie S6.
Intravital imaging of a neutrophil migrating in a skin capillary with a gradual confinement.

Movie S7.
Migration of mNeu in sharp size-transition channels.

Movie S8.
Migration of mNeu in channels with successive transitions.

Movie S9.
Migration of mNeu in funel-shaped channels.

Movie S10.
Migration of Lifeact-EGFP mNeu in sharp size-transition channels.

Movie S11.
Migration of Lifeact-EGFP mNeu in straight channels of different widths.

Movie S12.
Examples of Lifeact-GFP mNeu migrating in skin capillaries.

Movie S13.
Intravital imaging of endogenous neutrophils trafficking in liver sinusoids.

Movie S14.
Intravital imaging of Lifeact-GFP mNeu (injected) migration in liver sinusoids.

Movie S15.
Example of Lifeact-EGFP mNeu migration and deformation in liver sinusoid.

Movie S16.
Migration of MyoII-GFP mNeu in 2D confined chamber.

Movie S17.
Examples of MyoII-GFP mNeu migrating in large channels.

Movie S18.
Examples of MyoII-GFP mNeu migrating in sharp size-transition channels.

Movie S19.
Migration of Y-27632 treated mNeu in sharp size-transition channels.

Movie S20.
Calcium dynamics (Fluo8-AM) in mNeu migrating in sharp size-transition channels.

Movie S21.
Migration of control and ROCK-inhibited mNeu in networks of channels of different widths.

Data file S1. (separate file)
Uncropped immunoblot of fig.S3C.

Data file S2. (separate file)
Tabulated data underlying main figures.

Data file S3. (separate file)
Tabulated data underlying supplementary figures.